Hybrid renormalization for distribution amplitude of a light baryon in large momentum effective theory

Haoyang Bai,[1,2] Jun Hua,[3,4,*] Xiangdong Ji,[5] Xiangyu Jiang,[6] Jian Liang,[3,4] Andreas Schäfer,[7,8] Wei Wang,[9,10,†] Yi-Bo Yang,[6,11,12,13] Jian-Hui Zhang,[14] JiaLu Zhang,[15] Mu-Hua Zhang,[15] and Qi-An Zhang[16]

Lattice Parton Collaboration (LPC)

[1]*Institute of High Energy Physics, CAS, Beijing 100049, People's Republic of China*
[2]*School of Physics, University of Chinese Academy of Sciences, Beijing 100049, People's Republic of China*
[3]*State Key Laboratory of Nuclear Physics and Technology, Institute of Quantum Matter, South China Normal University, Guangzhou 510006, People's Republic of China*
[4]*Guangdong Basic Research Center of Excellence for Structure and Fundamental Interactions of Matter, Guangdong Provincial Key Laboratory of Nuclear Science, Guangzhou 510006, People's Republic of China*
[5]*Department of Physics, University of Maryland, College Park, Maryland 20742, USA*
[6]*CAS Key Laboratory of Theoretical Physics, Institute of Theoretical Physics, Chinese Academy of Sciences, Beijing 100190, People's Republic of China*
[7]*Institut für Theoretische Physik, Universität Regensburg, D-93040 Regensburg, Germany*
[8]*Department of Physics, National Taiwan University, Taipei, Taiwan 106, People's Republic of China*
[9]*State Key Laboratory of Dark Matter Physics, Key Laboratory for Particle Astrophysics and Cosmology (MOE), Shanghai Key Laboratory for Particle Physics and Cosmology, School of Physics and Astronomy, Shanghai Jiao Tong University, Shanghai 200240, People's Republic of China*
[10]*Southern Center for Nuclear-Science Theory (SCNT), Institute of Modern Physics, Chinese Academy of Sciences, Huizhou 516000, Guangdong Province, People's Republic of China*
[11]*School of Fundamental Physics and Mathematical Sciences, Hangzhou Institute for Advanced Study, UCAS, Hangzhou 310024, People's Republic of China*
[12]*International Centre for Theoretical Physics Asia-Pacific, Beijing/Hangzhou, People's Republic of China*
[13]*School of Physical Sciences, University of Chinese Academy of Sciences, Beijing 100049, People's Republic of China*
[14]*School of Science and Engineering, The Chinese University of Hong Kong, Shenzhen 518172, People's Republic of China*
[15]*State Key Laboratory of Dark Matter Physics, Key Laboratory for Particle Astrophysics and Cosmology (MOE), Shanghai Key Laboratory for Particle Physics and Cosmology, Tsung-Dao Lee Institute and School of Physics and Astronomy, Shanghai Jiao Tong University, Shanghai 200240, People's Republic of China*
[16]*School of Physics, Beihang University, Beijing 102206, People's Republic of China*

(Received 19 August 2025; accepted 25 November 2025; published 29 December 2025)

Light cone distribution amplitudes for a light baryon can be extracted through the simulation of the quasi-distribution amplitudes (quasi-DAs) on the lattice. We implement the hybrid renormalization for the quasi-DAs of light baryons. Lattice simulations are performed using $N_f = 2 + 1$ stout-smeared clover fermions and a tree-level Symanzik-improved gauge action, with three lattice spacings of 0.105, 0.077, 0.052 fm. By analyzing zero-momentum matrix elements for different lattice spacings, we extract the linear divergence associated with the Wilson-line self-energy. Matching to perturbative matrix elements in the $\overline{\text{MS}}$ scheme yields the residual self-renormalization factors. Using these factors, we renormalize the quasi-DAs

*Contact author: junhua@scnu.edu.cn
†Contact author: wei.wang@sjtu.edu.cn

within the hybrid scheme, which combines self-renormalization at large separations and the ratio scheme at short distances. The renormalized results demonstrate effective cancellation of linear divergences and yield smooth, continuumlike coordinate-space distributions suitable for subsequent Fourier transformation and perturbative matching. These results establish the viability of both self- and hybrid-renormalization frameworks for light baryon quasi-DAs, providing a robust foundation for LaMET-based determinations of light cone distribution amplitudes in future.

DOI: 10.1103/rqmb-x9x8

I. INTRODUCTION

Light baryons—particularly protons and neutrons—constitute the vast majority of visible matter in the Universe. Understanding their internal structure is one key objective in modern nuclear and particle physics, with profound implications for both theory and experiment. An important theoretical quantity for describing the internal dynamics of baryons at high energy are the baryon light cone distribution amplitudes (LCDAs), which encode the longitudinal momentum structure of valence quarks in the baryon.

Moreover, the LCDAs of light baryons serve as crucial nonperturbative inputs not only for predicting and interpreting CP-violating observables in weak decays of heavy bottom baryons, but also for the calculation of baryonic form factors and the exploration of possible signals of new physics. For instance, recently, the LHCb Collaboration reported the first experimental observation of CP violation in a baryonic decay channel, $\Lambda_b^0 \to pK^-\pi^+\pi^-$ [1], as well as previous evidence for CP violation in the decay $\Lambda_b^0 \to \Lambda K^+K^-$ [2]. This milestone result, along with anticipated high-precision measurements in future experiments, places increasing demands on the accuracy of theoretical inputs. Several related theoretical analyses and predictions can be found in Refs. [3–10]. In particular, in Ref. [10] a next-to-leading order analysis of the nucleon form factors using the first moments of baryon LCDAs from Ref. [11] is about an order of magnitude smaller than the experimental value. Moreover, the analyses in Refs. [6,7] show that parameter uncertainties in model parametrizations for LCDAs already lead to more than 30% uncertainties to physical observables like decay branching fractions and CP violations, while systematic uncertainties are yet unexplored. These observations strongly motivate developments of baryon LCDA studies from first-principles of QCD.

In contrast to the extensive studies of meson LCDAs-including a few moments [12,13] and x-dependent distributions [14–22] from lattice QCD, as well as phenomenological approaches such as QCD sum rules [23–26] and Dyson-Schwinger equations [27–29], the investigation of baryon LCDAs remains significantly less developed. The most commonly used estimates still originate from the Chernyak-Ogloblin-Zhitnitsky (COZ) model [30], proposed several decades ago within the QCD sum rule framework. Recently, several lowest moments of octet baryons have been computed on the lattice using the operator product expansion (OPE) [11,31,32], but these results remain insufficient for the precision required in phenomenological studies of baryonic decays.

In the past decade, several inspiring approaches have been proposed to calculate light cone distributions from lattice QCD, including the large-momentum effective theory (LaMET) [33,34], the pseudodistribution approach [35,36], and the lattice cross section method [37]. Among these, LaMET has proven particularly effective in enabling the extraction of fully x-dependent distribution amplitudes from Euclidean lattice data, and significant progress has been achieved in this framework [14,16,18–22,38–81]. Meanwhile, the pseudodistribution [82–92] and current-current correlation methods [93–97] have also produced many interesting and complementary results. Recently, the LaMET has been extended to the leading-twist LCDAs of baryons [98], where some preliminary results are given. In this analysis, the quasi-DAs are renormalized in a ratio scheme for both short-distance and long-distance spatial separations. To obtain robust results for baryon LCDAs, the renormalization of quasi-DAs for baryons still requires further study, particularly the development of a more systematic scheme to address linear divergences. Linear divergences pose a significant challenge to the renormalization of nonlocal operators on the lattice, making it difficult to directly extract light cone distributions from quasidistributions. In recent years, it has been noticed that the hybrid scheme and self-renormalization methods [47,53] enable the proper renormalization of nonlocal operators in lattice QCD. These developments have, in turn, facilitated precision LaMET calculations of hadronic distribution functions.

The hybrid renormalization scheme, combined with the self-renormalization method, determines the linear divergence by computing nonlocal operators at multiple lattice spacings and extracting the divergence through a parametrized fit of the zero momentum matrix elements. In the perturbative region, these results are then matched to the corresponding perturbative expressions in the $\overline{\text{MS}}$ scheme, yielding renormalization factors that allow conversion to the light cone scheme. In regions beyond the reach of lattice calculation, asymptotic extrapolation is introduced to circumvent the inverse problem associated with the limited Fourier transform. However, applying this hybrid scheme

TABLE I. The corresponding valence quark f, g, h for each light octet baryon.

Octet	n	p	Σ^-	Σ^0	Σ^+	Ξ^-	Ξ^0	Λ
fgh	d d u	u u d	d d s	$\frac{(uds+dus)}{\sqrt{2}}$	u u s	s s d	s s u	u d s

procedure to baryon LCDAs is significantly more challenging than in the meson cases, as the perturbative expressions for baryon LCDAs typically feature more pronounced physical peaks. This necessitates high-precision numerical simulations at short distances and makes the matching procedure substantially more intricate. In this work, we present a numerical implementation of the hybrid renormalization scheme for baryon LCDAs, laying a solid foundation for future precision calculations.

The rest of this paper is organized as follows. In Sec. II, we give the definition of the quasidistribution amplitudes (quasi-DAs) of light baryons and discuss their symmetry properties in coordinate space. Section III reviews the self-renormalization and the hybrid scheme for baryon quasi-DAs. The lattice simulation setup is described in Sec. IV. Numerical results for the self-renormalization procedure, as well as the renormalized quasi-DAs for both the Λ and the proton, are presented in Sec. V. The final section provides a summary and discusses prospects for future work.

II. QUASIDISTRIBUTION AMPLITUDES FOR LIGHT BARYON

A. Definitions of LCDAs and quasi-DAs for a light baryon

The baryon light cone distribution amplitudes are defined as the hadron-to-vacuum matrix elements of nonlocal three-quark operators at lightlike separations [99,100],

$$\begin{aligned} H(z_1,z_2,z_3)_{\alpha\beta\gamma} &= \epsilon^{ijk}\langle 0|f^{i'}_{\alpha}(z_1 n)W^{i'i}(z_1 n,z_0 n) \\ &\times g^{j'}_{\beta}(z_2 n)W^{j'j}(z_2 n,z_0 n) \\ &\times h^{k'}_{\gamma}(z_3 n)W^{k'k}(z_3 n,z_0 n)|B(P_B,\lambda)\rangle, \end{aligned} \tag{1}$$

where $|B(P_B,\lambda)\rangle$ represents a baryon state with momentum $P^{\mu}_B = P^+_B \bar{n}^{\mu} = (P^z_B, 0, 0, P^z_B)$ and helicity λ. These α,β,γ are Dirac indices. $i^{(\prime)}$, $j^{(\prime)}$, $k^{(\prime)}$ refer to color indices, and f, g, h are the quark fields in each baryon state, as shown in Table I. The lightlike Wilson lines W_{ij} connect different nonlocal quark fields to a general reference position z_0 to preserve gauge invariance. Two light cone unit vectors are defined as $n^{\mu} = (1,0,0,-1)/\sqrt{2}$ and $\bar{n}^{\mu} = (1,0,0,1)/\sqrt{2}$. The above structure can be depicted in Fig. 1 for light baryon LCDA.

The matrix element of the LCDAs for an octet baryon in Eq. (1) can be decomposed into three functions at leading twist (twist-3),

$$\begin{aligned} &\langle 0|f_{\alpha}(z_1 n)g_{\beta}(z_2 n)h_{\gamma}(z_3 n)|B(P_B)\rangle \\ &= \frac{1}{4}f_V[(\not{P}_B C)_{\alpha\beta}(\gamma_5 u_B)_{\gamma}V^B(z_i n\cdot P_B) \\ &\quad + (\not{P}_B\gamma_5 C)_{\alpha\beta}(u_B)_{\gamma}A^B(z_i n\cdot P_B)] \\ &\quad + \frac{1}{4}f_T(i\sigma_{\mu\nu}P^{\nu}_B C)_{\alpha\beta}(\gamma^{\mu}\gamma_5 u_B)_{\gamma}T^B(z_i n\cdot P_B), \end{aligned} \tag{2}$$

where $C \equiv i\gamma^2\gamma^0$ signifies the charge conjugation matrix and u_B stands for the baryon spinor.

Therefore, the different leading-twist components can be projected out from light cone nonlocal matrix elements as

$$\begin{aligned} &\Phi^B_V(z_i n\cdot P_B,\mu)(-f_V)P^+_B\gamma_5 u_B \\ &\quad = \langle 0|f^T(z_1 n)(C\not{n})g(z_2 n)h(z_3 n)|B(P_B)\rangle, \\ &\Phi^B_A(z_i n\cdot P_B,\mu)f_V P^+_B u_B \\ &\quad = \langle 0|f^T(z_1 n)(C\gamma_5\not{n})g(z_2 n)h(z_3 n)|B(P_B)\rangle, \\ &\Phi^B_T(z_i n\cdot P_B,\mu)(2f_T)P^+_B\gamma_5 u_B \\ &\quad = \langle 0|f^T(z_1 n)(iC\sigma_{\mu\nu}n^{\nu})g(z_2 n)\gamma^{\mu}h(z_3 n)|B(P_B)\rangle. \end{aligned} \tag{3}$$

where μ represents the renormalization scale. To simplify the notation, we can set z_3 to zero as shown in Fig. 1. With this convention, the LCDA generally defined in momentum space can be linked to the nonlocal matrix elements in light cone coordinates by Fourier transformation,

$$\begin{aligned} \phi_{V/A/T}(x_1,x_2,\mu) = &\int\frac{P^+_B dz_1}{2\pi}\int\frac{P^+_B dz_2}{2\pi} \\ &\times e^{i(x_1 z_1 + x_2 z_2)P^+_B}\Phi^B_{V/A/T}(z_1 n, z_2 n,\mu), \end{aligned} \tag{4}$$

where x_1 and x_2 denote the longitudinal momentum fractions of the f and g quarks, while the remaining quark h carries the fraction $x_3 = 1 - x_1 - x_2$, as shown in Fig. 2.

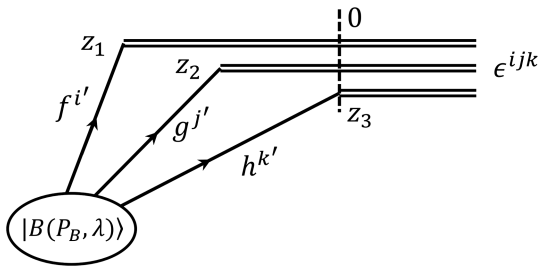

FIG. 1. The structure of the light baryon LCDA. Three quark fields are connected with Wilson lines to a reference position. z_3 can be set to zero for simplification.

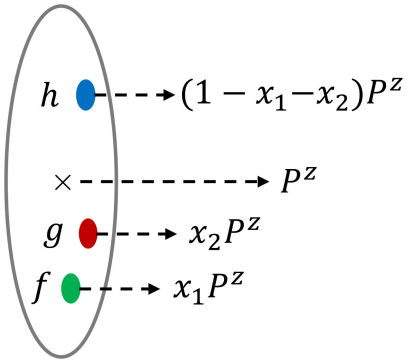

FIG. 2. The structure of a fast moving light baryon with valance quarks.

In this work, we focus on the leading-twist A-term ϕ_A^B of the Λ and the V-term ϕ_V^B of the proton, as these components remain nonvanishing in the local limit, as will be discussed in the following subsection.

Since lattice QCD cannot directly access timelike operators, an approach proposed by LaMET is to compute quasi-DAs defined in Euclidean space at finite but large hadron momentum. These quasi-DAs can then be matched to the corresponding LCDAs in the large momentum limit via an effective field theory framework. In Euclidean space, the leading-twist quasi-DAs of baryons are defined as follows:

$$\begin{aligned}
&\tilde{\Phi}_V^B(z_1,z_2,z_3,P_B^z,\mu)(-f_V)P_B^z\gamma_5 u_B \\
&\quad=\langle 0|f^T(z_1n_z)(C\gamma^\nu)g(z_2n_z)h(z_3n_z)|B(P_B)\rangle_R, \\
&\tilde{\Phi}_A^B(z_1,z_2,z_3,P_B^z,\mu)(f_A)P_B^z u_B \\
&\quad=\langle 0|f^T(z_1n_z)(C\gamma_5\gamma^\nu)g(z_2n_z)h(z_3n_z)|B(P_B)\rangle_R, \\
&\tilde{\Phi}_T^B(z_1,z_2,z_3,P_B^z,\mu)(2f_T)P_B^z\gamma_5 u_B \\
&\quad=\left\langle 0\left|f^T(z_1n_z)\frac{1}{2}C[\gamma^\nu,\gamma^\mu]g(z_2n_z)\gamma_\mu h(z_3n_z)\right|B(P_B)\right\rangle_R,
\end{aligned} \tag{5}$$

where n_z is a unit spacelike vector along the z direction, and P_B^z is the hadron momentum along the same direction. The subscript R refers to an appropriate nonperturbative renormalization scheme on the lattice.

The definition of the quasi-DA is very similar to the LCDA in Eq. (3), while the quark fields are separated by a Euclidean space distance z_i. The operator's Dirac structure can be chosen as $\gamma^\nu=\gamma^t$ or $\gamma^\nu=\gamma^z$, both approaching γ^+ in the large momentum limit. A possible origin of lattice artifacts for these operators is operator mixing effects. Unfortunately, no dedicated analysis of such effects exists. However, insights from quark bilinear operator studies in Refs. [40,61] indicate that γ^t-based operators exhibit less mixing than γ^z-based ones. For this reason, we choose $\gamma^\nu=\gamma^t$. Similarly, the momentum space quasi-DAs can be obtained from coordinate space matrix elements through a Fourier transformation,

$$\begin{aligned}
\tilde{\phi}_{V/A/T}(x_1,x_2,\mu)=&\int\frac{P^z dz_1}{2\pi}\int\frac{P^z dz_2}{2\pi} \\
&\times e^{-i(x_1z_1+x_2z_2)P^z}\tilde{\Phi}^B_{V/A/T}(z_1,z_2,\mu),
\end{aligned} \tag{6}$$

In lattice simulations, the ground state of nonlocal matrix elements of quasi-DAs in Eq. (5) can be extracted by reduction of the corresponding two-point correlation functions, defined as

$$\begin{aligned}
C_2(z_1,z_2;t,\vec{P})=&\int d^3x e^{-i\vec{P}\vec{x}}\langle 0|\hat{O}_{\text{Sink}}(\vec{x},t;z_1,z_2)_\gamma \\
&\times\bar{\hat{O}}_{\text{source}}(0,0;0,0)_{\gamma'}T^{\gamma\gamma'}|0\rangle,
\end{aligned} \tag{7}$$

where $T^{\alpha\beta}$ denotes the projection operator, which is optional for difference cases. The sink operator $\hat{O}_{\text{Sink}}(\vec{x},t;z_1,z_2)_\gamma$ depends on the specific leading-twist term $V/A/T$, as illustrated by the construction of the A-term operator,

$$\begin{aligned}
&\hat{O}^A_{\text{Sink}}(\vec{x},t;z_1,z_2)_\gamma \\
&\quad=\epsilon^{ijk}W^{ii'}(z_0,\vec{x}+z_1n_z)f_\alpha^{i'}(\vec{x}+z_1n_z,t) \\
&\qquad\times(C\gamma^t)_{\alpha\beta}W^{jj'}(z_0,\vec{x}+z_2n_z)g_\beta^{j'}(\vec{x}+z_2n_z,t) \\
&\qquad\times W^{kk'}(z_0,\vec{x})h_\gamma^{k'}(\vec{x},t).
\end{aligned} \tag{8}$$

Here, $W^{ij}(z_0,\vec{x})$ represents the spacelike Wilson line along the z direction. By setting the reference point z_0 at the h-quark position, it simplifies to

$$\begin{aligned}
&\hat{O}^A_{\text{Sink}}(\vec{x},t;z_1,z_2)_\gamma \\
&\quad=\epsilon^{ijk}W^{ii'}(\vec{x},\vec{x}+z_1n_z)f_\alpha^{i'}(\vec{x}+z_1n_z,t) \\
&\qquad\times(C\gamma^t)_{\alpha\beta}W^{jj'}(\vec{x},\vec{x}+z_2n_z)g_\beta^{j'}(\vec{x}+z_2n_z,t) \\
&\qquad\times h_\gamma^k(\vec{x},t).
\end{aligned} \tag{9}$$

B. Symmetries in baryon quasi-DAs

The quasi-DAs of the light octet baryons, defined as nonlocal matrix elements in Eq. (5), exhibit specific symmetry properties governed by their flavor structures. These symmetries can be utilized to streamline lattice computations. By treating the quasi-DAs $\tilde{\Phi}(z_1,z_2)$ as functions of the quark separation coordinates z_1 and z_2, we can distinguish different regions in the z_1-z_2 plane as shown in Fig. 3, to highlight the symmetry properties of the baryon quasi-DAs:

(i) The identical quark fields in the matrix elements induce symmetry under the exchange $z_1\leftrightarrow z_2$ for all octet baryons except Λ and Σ^0, where f and g are quarks of the same flavor. As a result, the three

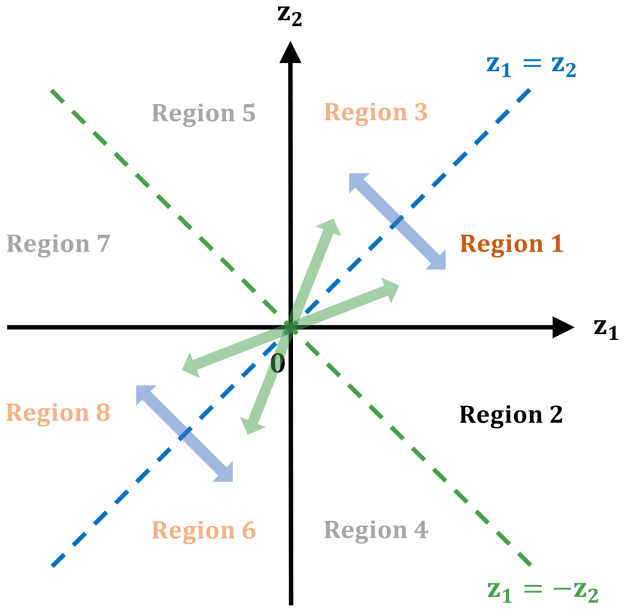

FIG. 3. The diagonals and regional divisions on the $z_1 - z_2$ plane for quasi-DAs.

structures V, A, T obey specific symmetries,

$$\begin{aligned}\tilde{\Phi}_V^B(z_1,z_2) &= \tilde{\Phi}_V^B(z_2,z_1),\\ \tilde{\Phi}_A^B(z_1,z_2) &= -\tilde{\Phi}_A^B(z_2,z_1),\\ \tilde{\Phi}_T^B(z_1,z_2) &= \tilde{\Phi}_T^B(z_2,z_1).\end{aligned} \tag{10}$$

(ii) After incorporating isospin symmetry where f and g are light quarks, additional constraints arise for the Λ and Σ^0,

$$\begin{aligned}\tilde{\Phi}_V^\Lambda(z_1,z_2) &= -\tilde{\Phi}_V^\Lambda(z_2,z_1),\\ \tilde{\Phi}_A^\Lambda(z_1,z_2) &= \tilde{\Phi}_A^\Lambda(z_2,z_1),\\ \tilde{\Phi}_T^\Lambda(z_1,z_2) &= -\tilde{\Phi}_T^\Lambda(z_2,z_1).\end{aligned} \tag{11}$$

$$\begin{aligned}\tilde{\Phi}_V^{\Sigma^0}(z_1,z_2) &= \tilde{\Phi}_V^{\Sigma^0}(z_2,z_1),\\ \tilde{\Phi}_A^{\Sigma^0}(z_1,z_2) &= -\tilde{\Phi}_A^{\Sigma^0}(z_2,z_1),\\ \tilde{\Phi}_T^{\Sigma^0}(z_1,z_2) &= \tilde{\Phi}_T^{\Sigma^0}(z_2,z_1).\end{aligned} \tag{12}$$

(iii) Another symmetry originates from the physical requirement that the LCDA in momentum space is pure real. Since the coordinate-space matrix elements are related to the momentum-space quasi-DAs via a Fourier transform,

$$\tilde{\Phi}(z_1,z_2,\mu) = \int_0^1 dx_1 \int_0^1 dx_2 e^{i(x_1 z_1 P^z + x_2 z_2 P^z)} \times \tilde{\phi}(x_1,x_2,\mu). \tag{13}$$

This imposes a complex-conjugation constraint,

$$\tilde{\Phi}(z_1,z_2) = \tilde{\Phi}^*(-z_1,-z_2). \tag{14}$$

Therefore, for the A-term of the Λ and V/T-terms of the proton, the identical symmetry properties in coordinate space can be illustrated with regions in Fig. 3 by the following equalities:

$$\begin{aligned}&\tilde{\Phi}_1(z_1,z_2) = \tilde{\Phi}_3(z_2,z_1) = \tilde{\Phi}_6^*(-z_2,-z_1) = \tilde{\Phi}_8^*(-z_1,-z_2),\\ &\tilde{\Phi}_2(z_1,z_2) = \tilde{\Phi}_4^*(-z_2,-z_1) = \tilde{\Phi}_5(z_2,z_1) = \tilde{\Phi}_7^*(-z_1,-z_2).\end{aligned} \tag{15}$$

For those V/T-terms of the Λ and A-term of the proton, the symmetry properties imply,

$$\begin{aligned}&\tilde{\Phi}_1(z_1,z_2) = -\tilde{\Phi}_3(z_2,z_1) = -\tilde{\Phi}_6^*(-z_2,-z_1) = \tilde{\Phi}_8^*(-z_1,-z_2),\\ &\tilde{\Phi}_2(z_1,z_2) = -\tilde{\Phi}_4^*(-z_2,-z_1) = -\tilde{\Phi}_5(z_2,z_1) = \tilde{\Phi}_7^*(-z_1,-z_2).\end{aligned} \tag{16}$$

Based on the symmetries discussed above, it is straightforward to see that only regions 1 and 2 in the z_1–z_2 plane are independent. Since our lattice simulation does not distinguish between u and d quarks, the quasi-DAs are strictly symmetric under the exchange $z_1 \leftrightarrow z_2$ as illustrated in Eqs. (10)–(12). These relations are satisfied on every individual configuration, thus allowing us to restrict calculations to the lower-right triangular region. In contrast to the flavor symmetries in Eqs. (10)–(12), the symmetry shown in Eq. (14) is a spacetime symmetry and holds after the configuration average. This symmetry stems from the fact that the matrix element is purely real in momentum space. On the lattice, the spacetime discretization and quantum fluctuations will disrupt this symmetry on each individual configuration. In our analysis, we will use the data both from regions 4 and 6 and from regions 1 and 2, and average over them.

In addition, Eqs. (15) and (16) can impose further constraints on the quasi-DAs. Specifically, Eq. (15) implies,

$$\mathrm{Im}\,[\tilde{\Phi}(z_1,z_2)]_{(z_1=-z_2)} \equiv 0, \tag{17}$$

while Eq. (16) leads to

$$\begin{aligned}[\tilde{\Phi}(z_1,z_2)]_{(z_1=z_2)} &\equiv 0,\\ \mathrm{Re}[\tilde{\Phi}(z_1,z_2)]_{(z_1=-z_2)} &\equiv 0.\end{aligned} \tag{18}$$

The corresponding consequence is that the V/T terms of the Λ and the A term of the proton vanish in the local limit. More properties of the V, A, T terms can be seen in Appendix A.

III. FRAMEWORK OF HYBRID RENORMALIZATION

A. Review of hybrid renormalization

In this work, we implement the hybrid renormalization method [47], a well-defined scheme for subtracting UV divergences without introducing extra nonperturbative effects at large distances. At short distances, it divides the large-momentum matrix element by the zero momentum matrix element (which defines the ratio scheme), which eliminates the UV divergences, introduces some of the perturbatively controllable z-dependences, and preserves the normalization of a distribution. At large distances, the renormalization factor extracted from self-renormalization [53] is introduced to cancel UV divergences, without introducing uncontrolled IR effects. Over the years this scheme has found a wide range of applications [18–22,56–58,74,101–113].

For the quasidistribution amplitudes of a light baryon, there are difficulties in applying the hybrid renormalization, both on the theoretical and numerical side. The theoretical issue arises from the mixing regions involving both short and large distances, such as ($|z_1| \ll 1/\Lambda_{\rm QCD}$ and $|z_2| \sim 1/\Lambda_{\rm QCD}$), ($|z_2| \ll 1/\Lambda_{\rm QCD}$ and $|z_1| \sim 1/\Lambda_{\rm QCD}$), or ($|z_1 - z_2| \ll 1/\Lambda_{\rm QCD}$, $|z_1| \sim 1/\Lambda_{\rm QCD}$ and $|z_2| \sim 1/\Lambda_{\rm QCD}$). In those regions, neither the ratio scheme nor self-renormalization can be simply used. However, as shown in one-loop perturbation theory [63,114,115], the UV logarithms $\ln(z_1^2)$, $\ln(z_2^2)$, and $\ln((z_1 - z_2)^2)$ are factorized out, which means that short and long distances can be treated independently in those mixing regions. Following the logic mentioned above, the hybrid renormalization designed for quasi distribution amplitudes of a light baryon has been proposed in [114], together with the hybrid counterterm at one loop.

The numerical issue lies in fitting the scheme conversion factor between the lattice calculations and perturbative calculations in the $\overline{\rm MS}$ scheme, which is performed in the short-distance region $0 < |z_1|, |z_2|, |z_1 - z_2| \ll 1/\Lambda_{\rm QCD}$, for continuum perturbation theory to work. This window hardly exists if the lattice spacing a is not small enough. Therefore, the ratio scheme is temporarily used in all regions in a preliminary study of baryon DA [98]. In this work, with more precise data at smaller lattice spacings a, we implement the hybrid renormalization, which avoids introducing extra nonperturbative effects compared to the ratio scheme.

B. Self-renormalization

Let us denote the bare lattice matrix element as $M(z_1, z_2, 0, P^z, a)$, which is related to Eq. (5) setting $z_3 = 0$ without subscript R. The normalized matrix element is denoted as $\hat{M}(z_1,z_2,0,P^z,a) = M(z_1,z_2,0,P^z,a)/M(0,0,0,P^z,a)$.

The starting point of the hybrid renormalization scheme is self-renormalization, which extracts the renormalization factor $Z_R(z_1, z_2, a, \mu)$ by converting the lattice data to the $\overline{\rm MS}$ scheme. The renormalization factor is an asymptotic series expansion at small lattice spacing with both logarithmic and power dependences, inspired by perturbation theory and parametrized as follows [114]:

$$\begin{aligned} Z_R(z_1, z_2, a, \mu) = \exp\Bigg[&\left(\frac{k}{a\ln[a\Lambda_{\overline{\rm QCD}}]} - m_0\right)\tilde{z} \\ &+ \frac{\gamma_0}{b_0}\ln\left[\frac{\ln[1/(a\Lambda_{\overline{\rm QCD}})]}{\ln[\mu/\Lambda_{\overline{\rm MS}}]}\right] \\ &+ \ln\left[1 + \frac{d}{\ln(a\Lambda_{\overline{\rm QCD}})}\right] + f(z_1, z_2)a^2\Bigg], \end{aligned} \tag{19}$$

where $(\frac{k}{a\ln[a\Lambda_{\overline{\rm QCD}}]} - m_0)\tilde{z}$ is the linear divergence [47,116–119] and the mass renormalization parameter [109,120–123], $\frac{\gamma_0}{b_0}\ln[\frac{\ln[1/(a\Lambda_{\overline{\rm QCD}})]}{\ln[\mu/\Lambda_{\overline{\rm MS}}]}] + \ln[1 + \frac{d}{\ln(a\Lambda_{\overline{\rm QCD}})}]$ contains the log divergence. $f(z_1, z_2)a^2$ contains discretization effects. In general the explicit forms of discretization effects depend on the details of the lattice action and the relevant operator. The lattice configuration has been generated with stout smeared clover fermion action and Symanzik gauge actions. Both the fermion and gauge actions are tadpole improved self-consistently and the anticipated discretization effects are $\mathcal{O}(a^2)$, see Ref. [124]. For the operators, the choice of an $\mathcal{O}(a^2)$ order parametrization is inspired by an analysis within lattice perturbation theory for the nonlocal operator with a Wilson line [116]. $\tilde{z}$ is the effective length for the linear divergence, which is defined as follows:

$$\tilde{z} = \begin{cases} |z_1 - z_2|, & z_1 z_2 < 0 \\ \max(|z_1|, |z_2|), & z_1 z_2 \geq 0. \end{cases} \tag{20}$$

The effective length $\tilde{z}$ can be justified by the effective length of Wilson links [98,114].

The parameters $b_0 = \frac{11C_A - 2n_f}{6\pi}$, $\gamma_0 = \frac{C_F}{2\pi}(5 - \frac{7}{4}\delta_{z_1,0} - \frac{7}{4}\delta_{z_2,0} - \frac{3}{2}\delta_{z_1-z_2,0})$ are determined from perturbation theory as shown in Ref. [114]. We use $\Lambda_{\overline{\rm MS}} = 0.338$ GeV for $n_f = 3$, as determined by FLAG2024 [125], in the running of the renormalized quantities to the $\overline{\rm MS}$ scheme. The parameters k, $\Lambda_{\overline{\rm QCD}}$, and $f(z_1, z_2)$ are obtained by fitting the a-dependence of the bare lattice data $\hat{M}(z_1, z_2, 0, P^z = 0, a)$. According to the study in Ref. [53], k and $\Lambda_{\overline{\rm QCD}}$ are strongly correlated. Therefore, a reasonable and convenient approach is to fix $\Lambda_{\overline{\rm QCD}}$ at a physically sensible value and fit k accordingly. In this work, we adopt $\Lambda_{\overline{\rm QCD}} = 0.2$ GeV. The parameters m_0 and d are calculated by matching the renormalized lattice data to perturbation theory at short distances,

$$\frac{\hat{M}(z_1,z_2,0,0,a)}{Z_R(z_1,z_2,a,\mu)}=\hat{M}_p(z_1,z_2,0,0,\mu), \tag{21}$$

where the perturbative zero-momentum matrix element $\hat{M}_p$ at one-loop is

$$\hat{M}_p(z_1,z_2,0,0,\mu)=1+\frac{\alpha_s C_F}{2\pi}\left[\frac{7}{8}\ln\left(\frac{z_1^2\mu^2e^{2\gamma_E}}{4}\right)+\frac{7}{8}\ln\left(\frac{z_2^2\mu^2e^{2\gamma_E}}{4}\right)+\frac{3}{4}\ln\left(\frac{(z_1-z_2)^2\mu^2e^{2\gamma_E}}{4}\right)+4\right], \tag{22}$$

which can be found in Ref. [114].

After extracting the renormalization factor $Z_R(z_1,z_2,a,\mu)$, the renormalized lattice matrix elements in $\overline{\text{MS}}$ scheme can be defined as

$$\hat{M}_{\overline{\text{MS}}}(z_1,z_2,0,P^z,\mu)=\frac{\hat{M}(z_1,z_2,0,P^z,a)}{Z_R(z_1,z_2,a,\mu)}, \tag{23}$$

which will be utilized to calculate the hybrid renormalization scheme matrix elements in the next subsection.

C. Implementation of hybrid renormalization for baryon quasi-DAs

After obtaining the renormalization parameters from the self-renormalization procedure, one can apply them to renormalize the bare nonlocal matrix elements of quasi-DAs with nonzero momentum. However, $Z_R(z_1,z_2,a,\mu)$ in self-renormalization will introduce peaks at $z_{1,2}=0$ and $z_2=z_1$, reflecting the short-distance logarithmic behavior of the perturbative quasi-DA. Such singularities not only impact the numerical quasi-DAs but also manifest in the matching kernel for converting the self-renormalized scheme to the light cone scheme, introducing intractability to both theoretical calculations and numerical processing [126]. To address these singularities in scheme conversions, we implement a hybrid renormalization scheme [47].

The hybrid renormalization scheme can be viewed as an improvement of self-renormalization, by combining the ratio scheme at short distances with the self-renormalization at large distances. Three typical regions exist in the hybrid renormalization method for baryons; the short-distance, large-distance, and mixing regions. As shown in [114], the overall matrix elements in the hybrid renormalization scheme for baryon quasi-DAs follow:

$$\begin{aligned}\hat{M}_H(z_1,z_2,0,P^z)=&\frac{\hat{M}_{\overline{\text{MS}}}(z_1,z_2,0,P^z,\mu)}{\hat{M}_{\overline{\text{MS}}}(z_1,z_2,0,0,\mu)}(\theta(2z_s-|z_1|)\theta(z_s-|z_2|)+\theta(z_s-|z_1|)\theta(|z_2|-z_s)\theta(2z_s-|z_2|))\\&+\frac{\hat{M}_{\overline{\text{MS}}}(z_1,z_2,0,P^z,\mu)}{\hat{M}_{\overline{\text{MS}}}(z_1,\text{sign}(z_2)2z_s,0,0,\mu)}\theta(z_s-|z_1|)\theta(|z_2|-2z_s)+\frac{\hat{M}_{\overline{\text{MS}}}(z_1,z_2,0,P^z,\mu)}{\hat{M}_{\overline{\text{MS}}}(\text{sign}(z_1)2z_s,z_2,0,0,\mu)}\theta(|z_1|-2z_s)\theta(z_s-|z_2|)\\&+\frac{\hat{M}_{\overline{\text{MS}}}(z_1,z_2,0,P^z,\mu)}{\hat{M}_{\overline{\text{MS}}}(z_s+(z_1-z_2)\theta(z_1-z_2),z_s+(z_2-z_1)\theta(z_2-z_1),0,0,\mu)}\theta(|z_1|-z_s)\theta(|z_2|-z_s)\theta(z_s-|z_1-z_2|)\\&+\frac{\hat{M}_{\overline{\text{MS}}}(z_1,z_2,0,P^z,\mu)}{\hat{M}_{\overline{\text{MS}}}(z_s+(z_1+z_2)\theta(z_1+z_2),-z_s+(z_2+z_1)\theta(-z_2-z_1),0,0,\mu)}\theta(|z_1|-z_s)\theta(|z_2|-z_s)\theta(z_s-|z_1+z_2|)\\&+\frac{\hat{M}_{\overline{\text{MS}}}(z_1,z_2,0,P^z,\mu)}{\hat{M}_{\overline{\text{MS}}}(\text{sign}(z_1)z_s,\text{sign}(z_2)2z_s,0,0,\mu)}\theta(|z_1|-z_s)\theta(|z_2|-z_s)\theta(|z_1-z_2|-z_s)\theta(|z_1+z_2|-z_s).\end{aligned} \tag{24}$$

Here, $\hat{M}_{\overline{\text{MS}}}(z_1,z_2,0,P^z,\mu)$ and $\hat{M}_{\overline{\text{MS}}}(z_1,z_2,0,0,\mu)$ represent the large-momentum and zero-momentum matrix elements, respectively, renormalized to the $\overline{\text{MS}}$ scheme using the self-renormalization factor Z_R. z_s is the hybrid cutoff chosen to satisfy $a\ll 2z_s\ll 1/\Lambda_{\text{QCD}}$. The θ functions are unit step functions that define region divisions and maintain continuity conditions. For example, $\theta(z_s-|z_1|)$ corresponds to the short distance interval $z_1\in[-z_s,z_s]$. Terms in the denominator such as $\text{sign}(z_1)z_s$ indicate the values at points $z_1=\pm z_s$, with the specific sign chosen to match the quadrant in which z_1 lies.

To carefully implement the hybrid renormalization in the three different regions above, we first partition the z_1–z_2 coordinate plane according to the perturbative and nonperturbative regimes of $|z_1|$, $|z_2|$, and $|z_1-z_2|$, while also considering $|z_1+z_2|$ for completeness. The regions are categorized as short-distance (perturbative), large-distance (nonperturbative), and mixing regions, as illustrated in Fig. 4. Then, we can apply different renormalization procedures in each region according to Eq. (24) with Fig. 4.

(i) *Short-distance region* (purple area in Fig. 4): For this region, we apply the ratio scheme,

$$\frac{\hat{M}_{\overline{\text{MS}}}(z_1,z_2,0,P^z,\mu)}{\hat{M}_{\overline{\text{MS}}}(z_1,z_2,0,0,\mu)}\cdot S_{\text{short}}(z_1,z_2), \tag{25}$$

where S_{short} is the step function defining the short-distance region,

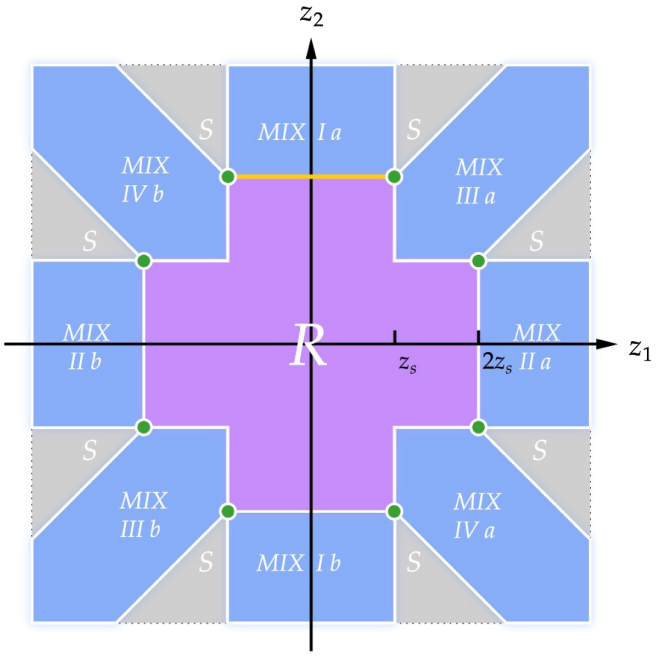

FIG. 4. A schematic diagram of renormalization regions. Distinct colors denote different region types; short-distance region (purple), long-distance region (gray), and mixing regions (blue). Separate renormalization schemes are applied to each region.

$$S_{\text{short}} = \theta(2z_s - |z_1|)\theta(z_s - |z_2|) + \theta(z_s - |z_1|)\theta(|z_2| - z_s)\theta(2z_s - |z_2|). \quad (26)$$

Here, we choose $z_s = 0.20$ fm which satisfies $a \ll 2z_s \ll 1/\Lambda_{\text{QCD}}$. This choice cancels singular logarithmic terms in the perturbative region while preserving normalization.

(ii) *Long-distance region* (gray areas in Fig. 4): We use the self-renormalized large momentum matrix element at this region,

$$\frac{\hat{M}_{\overline{\text{MS}}}(z_1, z_2, 0, P^z, \mu)}{\hat{M}_{\overline{\text{MS}}}(\text{sign}(z_1)z_s, \text{sign}(z_2)2z_s, 0, 0, \mu)} \cdot S_{\text{long}}(z_1, z_2), \quad (27)$$

where S_{long} is the step functions to separate the short or medium distance and long distance regions, and combining with the denominator to address the continuity condition,

$$S_{\text{long}} = \theta(|z_1| - z_s)\theta(|z_2| - z_s) \times \theta(|z_1 - z_2| - z_s)\theta(|z_1 + z_2| - z_s). \quad (28)$$

The value in the denominator is the self-renormalized zero-momentum matrix elements at inner boundary points of the gray region (green points in Fig. 4), which ensures continuity with the ratio scheme. Here we can only consider the results on four points $(\text{sign}(z_1)z_s, \text{sign}(z_2)2z_s)$ in Eq. (27). The other four points can be derived based on the isospin symmetry shown in Eq. (15).

(iii) *Mixing regions* (blue areas in Fig. 4): In these regions, one of the nonlocal separation directions lies within the perturbative regions while the others do not. For example, in the blue vertical region *MIX I a* (z_1 is perturbative, while z_2 and $|z_1 - z_2|$ are nonperturbative). We will introduce the ratio scheme for z_1 and the self-renormalization for z_2 within this region, as shown in the following equation:

$$\frac{\hat{M}_{\overline{\text{MS}}}(z_1, z_2, 0, P^z, \mu)}{\hat{M}_{\overline{\text{MS}}}(z_1, \text{sign}(z_2)2z_s, 0, 0, \mu)} \cdot \theta(z_s - |z_1|)\theta(|z_2| - 2z_s). \quad (29)$$

The numerator part represents the self-renormalized large-momentum matrix elements in this region, while the denominator part represents the self-renormalized zero-momentum matrix elements on the boundary line between the self-renormalization region and the perturbative region (yellow line in Fig. 4). Therefore, the ratio at identical short-distance z_1 dependence cancels the $\ln(z_1^2)$ singularities. The z_2 dependence in the numerator is handled by self-renormalization, while the denominator truncates z_2-dependence at $\text{sign}(z_2)2z_s$, avoiding extra nonperturbative effects. Similar treatments apply to other blue regions,

$$\begin{aligned}
&\frac{\hat{M}_{\overline{\text{MS}}}(z_1, z_2, 0, P^z, \mu)}{\hat{M}_{\overline{\text{MS}}}(\text{sign}(z_1)2z_s, z_2, 0, 0, \mu)}\theta(|z_1| - 2z_s)\theta(z_s - |z_2|) \\
&+ \frac{\hat{M}_{\overline{\text{MS}}}(z_1, z_2, 0, P^z, \mu)}{\hat{M}_{\overline{\text{MS}}}(z_s + (z_1 - z_2)\theta(z_1 - z_2), z_s + (z_2 - z_1)\theta(z_2 - z_1), 0, 0, \mu)}\theta(|z_1| - z_s)\theta(|z_2| - z_s)\theta(z_s - |z_1 - z_2|) \\
&+ \frac{\hat{M}_{\overline{\text{MS}}}(z_1, z_2, 0, P^z, \mu)}{\hat{M}_{\overline{\text{MS}}}(z_s + (z_1 + z_2)\theta(z_1 + z_2), -z_s + (z_2 + z_1)\theta(-z_2 - z_1), 0, 0, \mu)}\theta(|z_1| - z_s)\theta(|z_2| - z_s)\theta(z_s - |z_1 + z_2|). \quad (30)
\end{aligned}$$

TABLE II. Key parameters for the simulations on the three lattice ensembles. Statistics $N_{\mathrm{cfg}} \times N_{\mathrm{src}}$ denotes the number of measurements on each ensemble.

Parameter	C24P29	F32P30	H48P32
Volume ($n_s^3 \times n_t$)	$24^3 \times 72$	$32^3 \times 96$	$48^3 \times 144$
a (fm)	0.10530(18)	0.07746(18)	0.05187(26)
m_π (MeV)	292.7(1.2)	303.2(1.3)	317.2(0.9)
m_K (MeV)	509.4(1.1)	524.6(1.8)	536.1(3.0)
Statistics ($N_{\mathrm{cfg}} \times N_{\mathrm{src}}$)	864×4	777×4	555×6

IV. SIMULATION SETUP

A. Lattice setup

The numerical simulations in this work are based on the $N_f = 2 + 1$ flavor gauge ensembles generated by the CLQCD Collaboration [124]. These ensembles have been extensively validated in previous studies of hadron spectroscopy [127–129], heavy meson physics [130,131], and nucleon structure [111]. In this work, we use three ensembles with lattice spacings of $a = \{0.105, 0.077, 0.052\}$ fm, which allow for self-renormalization and systematic control for discretization effects. More details are summarized in Table II.

To improve data quality at large momenta, we employ point-source propagators with momentum smearing [132]. To check the renormalization for both small and large momentum, we compute the quasi-DAs at three different momenta,

$$\begin{aligned} \text{C24P29}&: P^z = \{0, 0.49, 1.96\}\ \text{GeV}, \\ \text{F32P30}&: P^z = \{0, 0.50, 2.00\}\ \text{GeV}, \\ \text{H48P32}&: P^z = \{0, 0.50, 1.99\}\ \text{GeV}. \end{aligned}$$

The zero-momentum case is used to extract renormalization factors, while the nonzero-momentum cases serve to examine the behavior of the renormalized quasi-DAs.

In addition, to enhance the signal-to-noise ratio at large z-separations, we apply single-step hypercubic (HYP) smearing [133,134] to the spatial Wilson lines. It is important to note that HYP smearing modifies the linear divergence of the system, which is handled through self-renormalization. In Appendix B, we demonstrate that quasi-DAs with different iterations of HYP smearing, despite having distinct linear divergences, yield consistent results after renormalization.

B. Interpolators and projection operators

To extract the ground state of the hadron-to-vacuum matrix elements defined in Eq. (7), we construct a separate set of composite quark operators at the source side. The structure of the sink side is already fixed by the leading-twist structure Eq. (5) of the baryon LCDAs. To optimize the signal-to-noise ratio (SNR) and better extract the ground state while suppressing the excited-state contamination, we adopt two distinct strategies tailored to different momenta.

For small boost momenta, we typically choose the following operator combinations as interpolators for protons and Λ baryons:

$$\begin{aligned} \bar{O}^P &= (u^T C\gamma_5 d)u, \\ \bar{O}^\Lambda &= \frac{2(u^T C\gamma_5 d)s + (u^T C\gamma_5 s)d + (s^T C\gamma_5 d)u}{\sqrt{6}}. \end{aligned} \tag{31}$$

Inspired by Ref. [135], for the highly boosted momenta ($P^z \geq 2$ GeV), we adopt the modified interpolating operators that are constructed to better overlap with the leading Fock state in the boosted frame,

$$\begin{aligned} \bar{O}^P_{\mathrm{mod}} &= (u^T C\gamma_5\gamma^t d)u, \\ \bar{O}^\Lambda_{\mathrm{mod}} &= \frac{2(u^T C\gamma_5\gamma^t d)s + (u^T C\gamma_5\gamma^t s)d + (s^T C\gamma_5\gamma^t d)u}{\sqrt{6}}. \end{aligned} \tag{32}$$

In Fig. 5, we show an SNR comparison for large-momentum two-point correlation functions with the typical source interpolator and the modified operator.

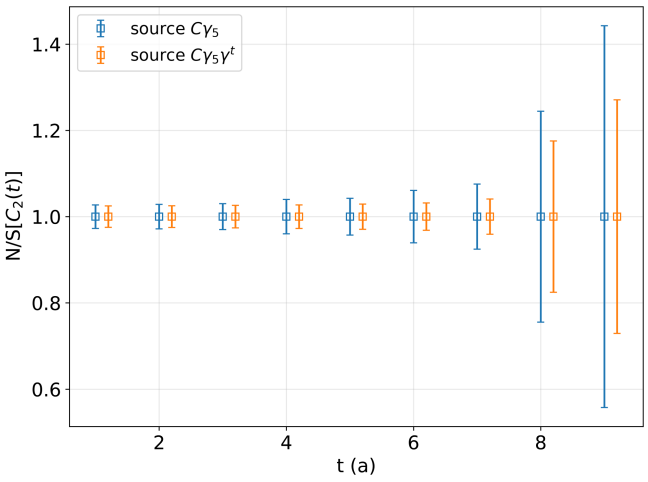

FIG. 5. Comparison of noise-to-signal ratios for the Λ baryon two-point functions at $P^z = 2.5$ GeV and F32P30 ($a = 0.077$ fm) using traditional [Eq. (31)] and modified [Eq. (32)] source interpolators.

TABLE III. Baryon interpolators and projection operators for different boosted momenta.

Momentum	Baryon	Interpolator	Projection
$P^z = 0,\ 1$	Proton	$(u^T C\gamma_5 d)u$	$(I+\gamma^t)/2$
	Λ	$\frac{(2(u^T C\gamma_5 d)s+\cdots)}{\sqrt{6}}$	
$P^z \geq 4$	Proton	$(u^T C\gamma_5\gamma^t d)u$	$\gamma^t+\gamma^z$
	Λ	$\frac{(2(u^T C\gamma_5\gamma^t d)s+\cdots)}{\sqrt{6}}$	

For the two-point baryon correlation functions, the projection operator $T^{\gamma\gamma'}$ shown in Eq. (7) is also required for matrix components. Conventionally, the projection operator $T=(I+\gamma^t)/2$ has been widely used in studies of light octet baryons at zero momentum, as it eliminates contributions from negative-parity excited states while projecting onto positive-parity states, including the ground state.

However, with nonzero momentum, the parity can no longer be easily identified through operator constructions, as contributions from states of different parity become mixed. Unlike the zero-momentum case, it is no longer possible to use a fixed projection operator to isolate only the positive-parity states; we can only ensure that the ground state corresponds to the desired positive-parity baryon. Therefore, at large momenta, the choice of projection operator is no longer unique. Instead, we can employ different projection operators and combine them to better extract the ground-state of leading twist.

In summary, our lattice simulation of two-point correlation function employs the following baryon interpolators and projection operators, as listed in Table III.

C. Extraction of ground-state matrix elements

To better suppress the excited-state contamination and reliably extract the ground-state contribution, we perform a two-state fit to the two-point correlation functions in this work. The parametrization follows:

$$\begin{aligned} C_2^{\mathrm{norm}}(z_1,z_2;t,P^z) &= \frac{C_2(z_1,z_2;t,P^z)}{C_2(0,0;t,P^z)} \\ &= \tilde{\Phi}(z_1,z_2,P^z)(1+\Delta A(z_1,z_2,P^z)e^{-\Delta E\cdot t}), \end{aligned} \tag{33}$$

where $\tilde{\Phi}(z_1,z_2,P^z)$ represents the ground-state matrix element, and the $\Delta A e^{-\Delta E\cdot t}$ term accounts for excited-state contamination. However, it is well known that this fit can be sensitive to the fit range in time t. The comparison of one-state (constant) and two-state fits with different fit ranges of t is shown in Fig. 6.

To systematically address the fit-range dependence, we implement the model averaging procedure introduced in Ref. [136], instead of a two-state fit with fixed range. This approach can combine two-state fit results over different fit ranges $[t_{\mathrm{min}}, t_{\mathrm{max}}]$, with weights for each fit range determined by both the fit quality (χ^2/d.o.f.) and the initial point t_{min}, as shown in Eq. (35). The weighted average result and its uncertainty are given by

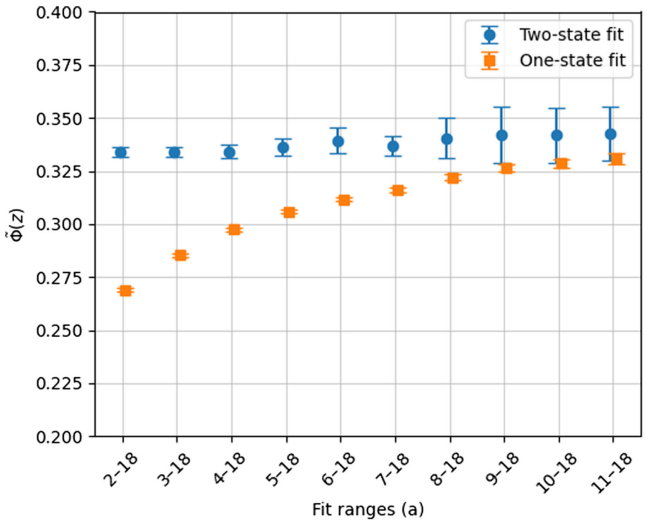

FIG. 6. Comparison of one-state (constant) and two-state fits for the ground-state quasi-DAs on the normalized two-point function at $\{z_1,z_2,P^z\}=\{6a,2a,0.5\ \mathrm{GeV}\}$ of F32P30 ($a=0.077$ fm).

$$\bar{\Psi}=\sum_i w_i\Psi_i, \qquad \sigma_{\bar{\Psi}}^2=\sum_i w_i\Psi_i^2-\bar{\Psi}^2+w_i\sigma_i^2, \tag{34}$$

$$w_i \propto \exp\left(-\frac{1}{2}\chi_i^2-t_{\mathrm{min}}^{(i)}\right), \tag{35}$$

where Ψ_i and σ_i^2 are the result and uncertainty of each fit, $t_{\mathrm{min}}^{(i)}$ represents the initial time point of each fit, w_i are the weights to average all cases. This method accounts for potential systematic uncertainties arising from the choice of fit ranges while avoiding artificially inflated errors. An example comparing the model-averaged fit with two-state fits over different t ranges is shown in Fig. 7. The upper panel displays the matrix elements extracted from the ground state using various fit strategies, and the lower panel shows the corresponding weights assigned to different values t_{min} in the model averaging procedure.

This combined approach (two-state fitting with model averaging) yields stable extractions of ground-state matrix elements and reliable uncertainty estimates, enabling a reliable determination of the quasi-DA matrix elements necessary for the subsequent renormalization and matching procedures. An example of the fitting results using this method is shown in Fig. 8. Therefore, we will use the quasi-DA matrix elements determined by this method in the following analysis.

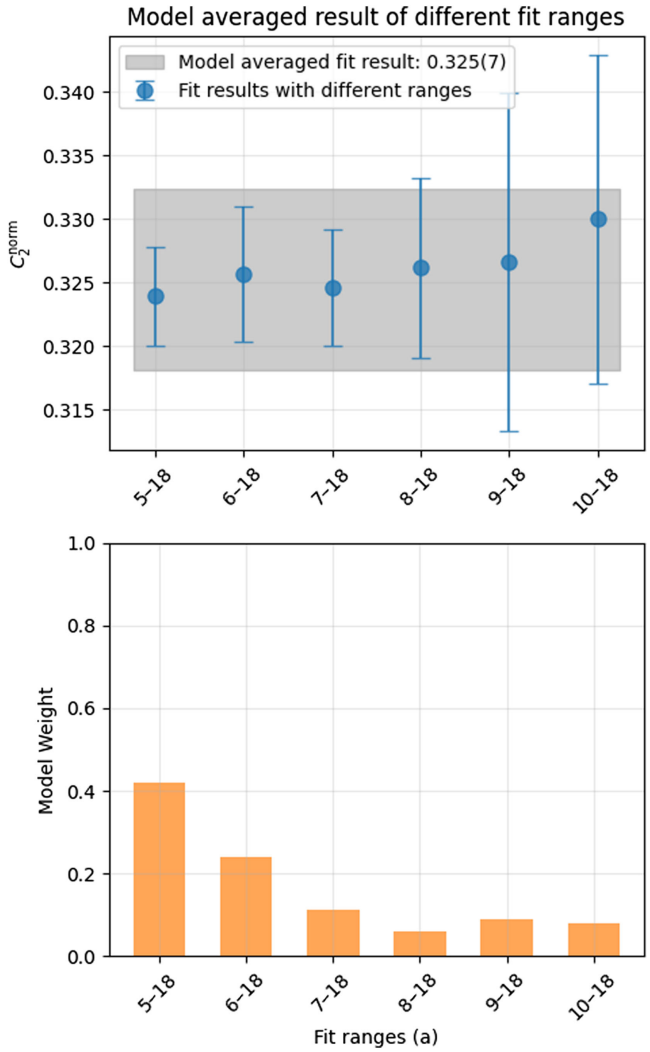

FIG. 7. Model averaging of Λ ground-state matrix elements at $\{z_1, z_2, P^z\} = \{6a, 0a, 0.5\ \text{GeV}\}$ for F32P30 ($a = 0.077$ fm): (Upper) Fit results for different fit ranges (colored points) and weighted average result with total uncertainty including systematics (gray band); (Lower) Corresponding weights w_i (bars) of each fit range.

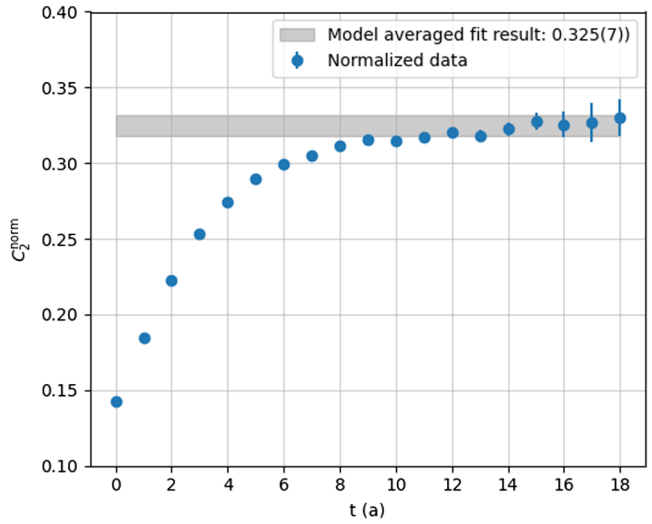

FIG. 8. Result of the model-averaged two-state fit on normalized matrix element of Λ at $\{z_1, z_2, P^z\} = \{6a, 0a, 0.5\ \text{GeV}\}$ for F32P30 ($a = 0.077$ fm). The colored points are the normalized data while the gray band shows the model averaged fitting result.

D. Dispersion relation

Since our study involves two-point functions at large momenta, we examine the dispersion relation to assess both discretization effects and the reliability of the calculation. The effective energies $E(P^z)$ are extracted from the local two-point correlation functions [Eq. (7)] at local points $z_1 = z_2 = 0$ by applying the model-averaged two-state fit for both the Λ and the proton, with the highest boosted momenta up to $P^z = 7 \times 2\pi/(n_s a) \simeq 3.5$ GeV on all three ensembles.

The dispersion relations are quantified through the parametrization,

$$E^2 = m_B^2 + c_0 (P^z)^2 + c_1 a^2 (P^z)^4, \tag{36}$$

where c_0 and c_1 parametrize deviations from the continuum relativistic expectation $E^2 = m_B^2 + (P^z)^2$. Figure 9 displays the results for the three ensembles.

We find that the values of c_0 and c_1 are consistent with the continuum expectation within 3σ. The slight deviation of c_0 from 1 is primarily due to complicated excited-state contamination of the Λ and the proton, while the deviation of c_1 from 0 reflects discretization effects. Moreover, the results exhibit a trend towards the continuum limit as the lattice spacing decreases, providing theoretical support for the subsequent continuum extrapolation.

V. NUMERICAL APPLICATION FOR HYBRID RENORMALIZATION

As discussed in the framework of hybrid renormalization, lattice calculations involving nonlocal operators suffer from linear divergences. These divergences manifest themselves as significant deviations in the computed values of the same physical quantity at different lattice spacings. In the cases of baryon quasi-DAs, which involve nonlocal separations in two directions, we illustrate the impact of linear divergence more clearly by fixing either z_1 or z_2. As shown in Fig. 10, Fig. 10(a) presents the bare quasi-DA of the Λ baryon at fixed $z_1 = 0$, while Fig. 10(b) shows the case with $z_1 = z_2$. One can observe significant differences among the results obtained at three different lattice spacings, far exceeding the expectations of discretization effects. Therefore, a proper renormalization of linear divergences is essential to ensure reliable matching to the $\overline{\text{MS}}$ scheme and to obtain a meaningful continuum limit. To facilitate comparison and enable consistent analysis of lattice spacing dependence within the self-renormalization scheme, we interpolate the bare matrix

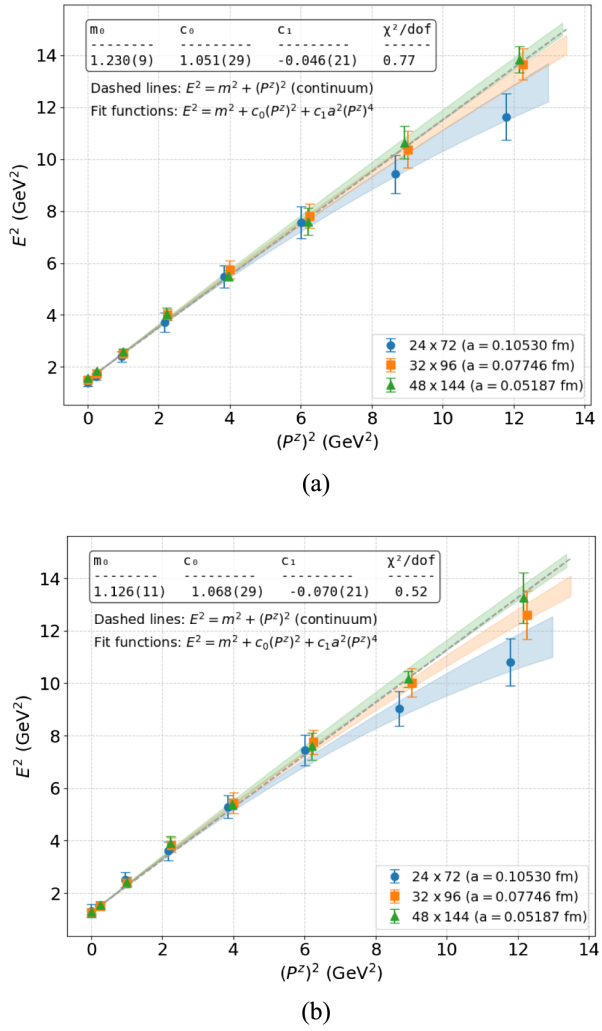

FIG. 9. Dispersion relations for the (a) Λ baryon and (b) the proton on C24P29 ($a = 0.105$ fm), F32P30 ($a = 0.077$ fm), and H48P32 ($a = 0.052$ fm). The dashed lines show the continuum relativistic prediction $E^2 = m_\Lambda^2 + (P^z)^2$.

element results from each ensemble onto a common grid with a spacing of 0.05 fm.

A. Linear and logarithmic divergence extraction

The matrix element of a baryon quasi-DA can be parametrized as

$$M(z_1, z_2, a, \mu) = \exp\left[\left(\frac{k}{a\ln[a\Lambda_{\overline{\rm QCD}}]}\right)\tilde{z} + g(z_1, z_2) + \frac{\gamma_0}{b_0}\ln\left[\frac{\ln[1/(a\Lambda_{\overline{\rm QCD}})]}{\ln[\mu/\Lambda_{\overline{\rm MS}}]}\right] + \ln\left[1 + \frac{d}{\ln(a\Lambda_{\overline{\rm QCD}})}\right] + f(z_1, z_2)a^2\right], \tag{37}$$

which is similar to Eq. (19), but with

$$g(z_1, z_2) = \ln[\hat{M}_{\overline{\rm MS}}(z_1, z_2, 0, 0, \mu) + m_0\tilde{z}]. \tag{38}$$

Here $\hat{M}_{\overline{\rm MS}}(z_1, z_2, 0, 0, \mu)$ is the numerical zero-momentum matrix elements in $\overline{\rm MS}$ scheme, which is consistent with the perturbative $\hat{M}_p(z_1, z_2, 0, 0, \mu)$ at short distance. The $\overline{\rm MS}$ renormalization scale μ is chosen as $\mu = 2$ GeV in our following analysis.

From the analytical expression for the matrix element Eq. (37), it is obvious that for a given nonlocal matrix element, when the separation z is relatively large while the lattice spacing is small, the dominant contribution in the matrix element arises from the linear divergence. To better illustrate both the impact of this linear divergence on the numerical lattice data, we can examine the dependence of the matrix elements on $1/a$ using a logarithmic scale. As shown in Fig. 11, both the Λ and the proton exhibit a clear linear dependence on 1/a. Since the baryon LCDA involves two nonlocal separations, z_1 and z_2, we present several representative cases with fixed $z_1 = -0.20$ fm, respectively, to illustrate the linear behavior, more cases are shown in Appendix C.

Therefore, following the analytical parametrization form in Eq. (37), we perform a global fit to the numerical matrix elements of the quasi-DAs. Compared to the meson case, which involves only a single nonlocal separation direction, the baryon quasi-DA features two nonlocal separation directions, imposing stronger constraints on determining the linear divergence parameter. This also provides more flexibility in selecting the fitting region, allowing us to avoid potential lattice artifacts, such as discretization effects. Specifically, we use the region satisfying $|z_{1,2}|, |z_1 - z_2| > 0.15$ fm to fit the linear divergence. The extracted linear divergence parameters for the Λ and the proton are $k^\Lambda = 0.779(03)$ with $\chi^2/\text{d.o.f.} = 1.0$, and $k^P = 0.781(05)$ with $\chi^2/\text{d.o.f.} = 0.9$, respectively. These consistent values indicate that the linear divergence is largely independent of the external state. More consistency checks of linear divergence can be seen in the Appendix C. Therefore, we take the extracted linear divergence values $k^{\Lambda,P}$ and perform self-renormalization for the Λ and the proton separately.

To further extract the renormalization parameters required for self-renormalization, one needs to match the lattice-calculated quasi-DA to the perturbative expression in the $\overline{\rm MS}$ scheme within the perturbative region, as discussed in Eq. (22). The matching is performed in the short-distance region to allow the application of perturbation theory. It is important to note that the perturbative expressions exhibit peaks at $z_1 = z_2$, while the numerical lattice data are smooth and continuous for all regions.

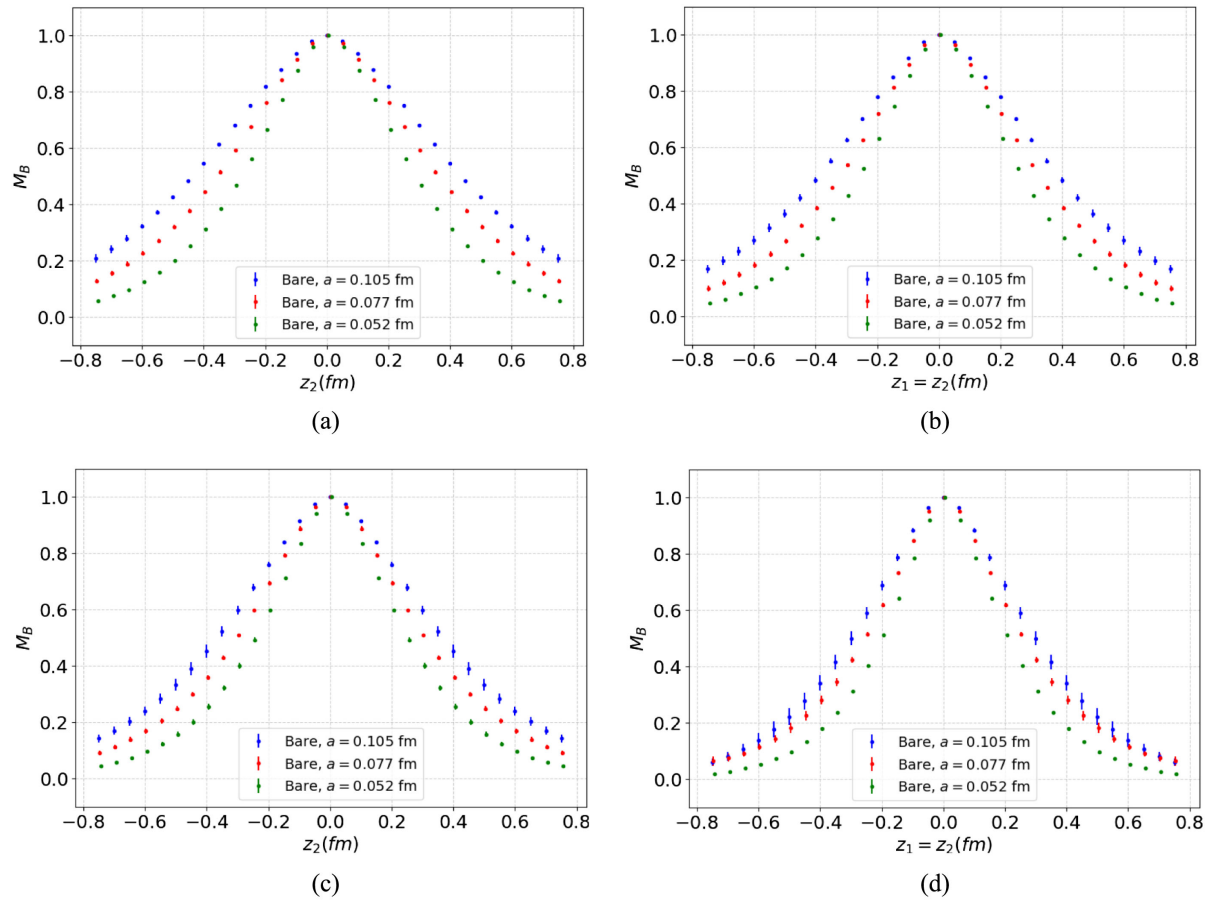

FIG. 10. Normalized bare zero-momentum quasi-DA for the proton and the Λ at three different lattice spacings. (a) Λ, $z_1 = 0$, (b) Λ, $z_1 = z_2$, (c) proton, $z_1 = 0$, (d) proton, $z_1 = z_2$.

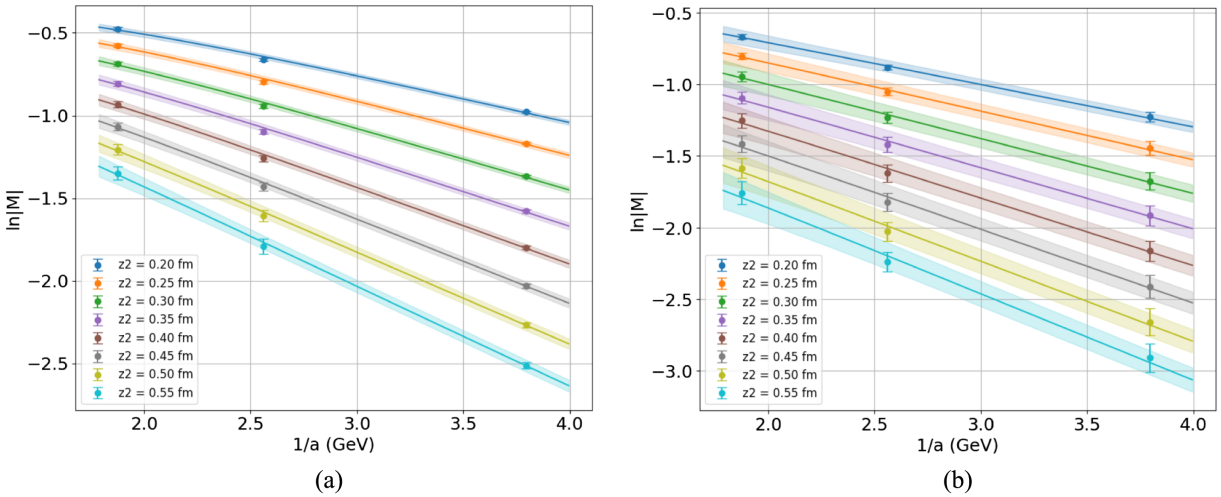

FIG. 11. Extraction of the linear divergence with lattice spacing dependence on zero-momentum matrix elements of the (a) Λ and (b) proton at $z_1 = -0.20$ fm.

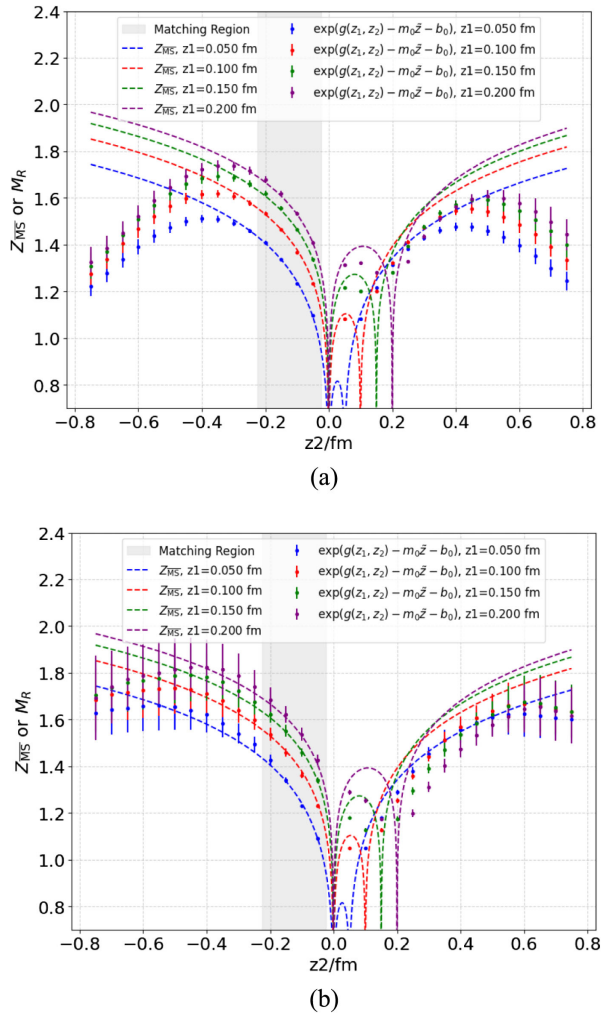

FIG. 12. The fitting result of the lattice matrix elements to the $\overline{\rm MS}$ scheme perturbative one-loop result in the perturbative region for the (a) Λ and (b) proton.

It makes the matching between discrete lattice data and the continuum expressions particularly challenging, not only for the discrete points along $z_1 = z_2$ but also for those nearby. To suppress the impact of perturbative peaks on the matching, we fit the data from quadrants II and IV. The extracted renormalization parameters are general and can be applied to test cases in quadrants I and III, including $z_1 = z_2$. As shown in Fig. 12, for the cases with $z_1 = 0.05$, 0.10, 0.15, 0.20 fm, the lattice data for both the Λ and the proton agree well with the perturbative zero-momentum matrix elements when $z_2 < 0$. However, for $z_2 > 0$, only the data points away from the $z_1 = z_2$ region show good agreement with the perturbative results, for example, $z_1 = 0.05$ with $z_2 = 0.15$, 0.20 fm, or $z_1 = 0.20$ with $z_2 = 0.05$ fm. The renormalization parameters extracted and applied in Fig. 12 are $m_0^\Lambda = 0.859(09)$ with $d^\Lambda = 0.476(04)$ for the Λ and $m_0^P = 0.073(22)$ with $d^P = 0.381(09)$ for the proton.

B. Hybrid renormalization results for baryon quasi-DA

With the above fitting process, we can extract the self-renormalization factor $Z_R(z_1, z_2, a, \mu)$ from the zero-momentum matrix elements and then use it to renormalize large-momentum matrix elements, yielding the self-renormalized quasi-DA. In Figs. 13 and 14, we show the comparison of bare, ratio renormalized and self-renormalized matrix elements in subfigures (a)–(c) for the Λ with both $P^z = 0.5$ GeV and $P^z = 2.0$ GeV.

As evident from these figures, the ratio scheme results exhibit continuity and smoothness across all regions, because taking the ratio to the zero-momentum matrix elements eliminates both short-distance logarithms and UV divergences. However, this division inevitably introduces nonperturbative IR effects at large distances. The self-renormalized results demonstrate effective removal of UV divergences at large distances without introducing additional uncontrollable nonperturbative effects. Yet at short distances, the self-renormalized results exhibit two peaks at $z_2 = 0$ and $z_2 = z_1$, reflecting the short-distance behavior of the perturbative quasi-DA as discussed before. This issue naturally leads us to employ the hybrid renormalization framework discussed in Sec. III C.

The hybrid renormalization is implemented as follows. After extracting the self-renormalization factor $Z_R(z_1, z_2, a, \mu)$ from the zero-momentum matrix elements, this factor is applied to renormalize both large-momentum and zero-momentum matrix elements, yielding $\hat{M}_{\overline{\rm MS}}(z_1, z_2, 0, P^z, \mu)$ and $\hat{M}_{\overline{\rm MS}}(z_1, z_2, 0, 0, \mu)$. Then perform region-specific ratios as previously described in Sec. III to achieve continuous hybrid renormalization scheme results.

The hybrid renormalized results for the Λ quasi-DA matrix elements at $P^z = 0.5$ GeV and $P^z = 2.0$ GeV are shown in subfigures (d) of Figs. 13 and 14. Compared to the self-renormalized results [Figs. 13(c) and 14(c)], the hybrid renormalization scheme effectively eliminates the singularities in the short-distance region. In the long-distance region, it naturally transitions to self-renormalization, which provides optimal UV divergence removal. Crucially, the hybrid renormalized results exhibit smooth continuity across the transition regions while retaining proper normalization, which facilitates subsequent limited Fourier transforms [81,137] and effective matching procedures. The corresponding results for the proton quasi-DA are presented in Appendix D.

Figures 15 and 16 display 2D heat maps of hybrid renormalized quasi-DA matrix elements (central values) for the Λ (A-term) and the proton (V-term) across all four quadrants at $P^z = 2.0$ GeV. These visualizations further demonstrate the smoothness and continuity of the hybrid renormalized results over the entire coordinate space. Moreover, the quasi-DAs at 2 GeV exhibit a clear and

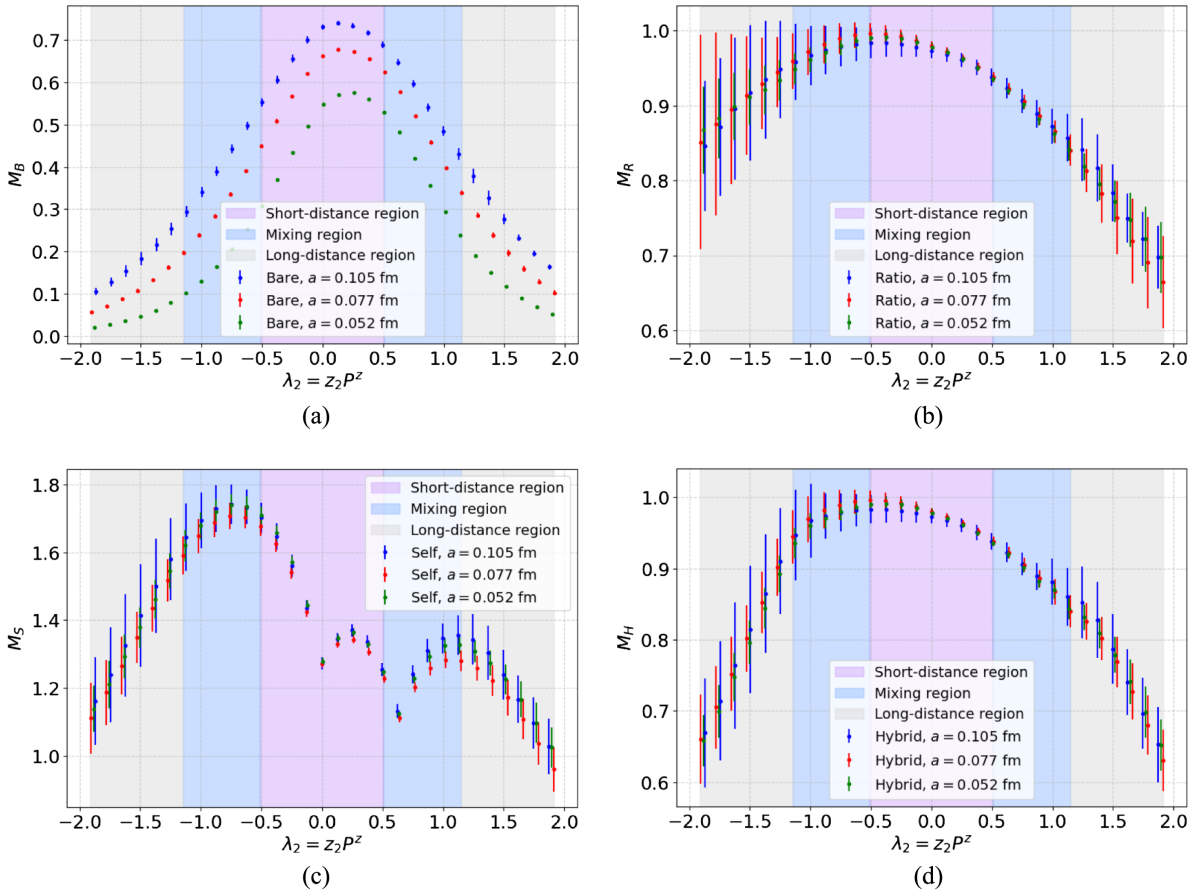

FIG. 13. Bare, ratio scheme, self-renormalized and hybrid renormalization scheme results of the Λ quasi-DA matrix elements at $P^z = 0.5$ GeV, fix $z_1 = 0.250$ fm ($\lambda_1 = 0.631$). (a) Bare result of Λ at $P = 0.5$ GeV. (b) Ratio scheme result of Λ at $P = 0.5$ GeV. (c) Self-renormalized result of Λ at $P = 0.5$ GeV. (d) Hybrid scheme result of Λ at $P = 0.5$ GeV.

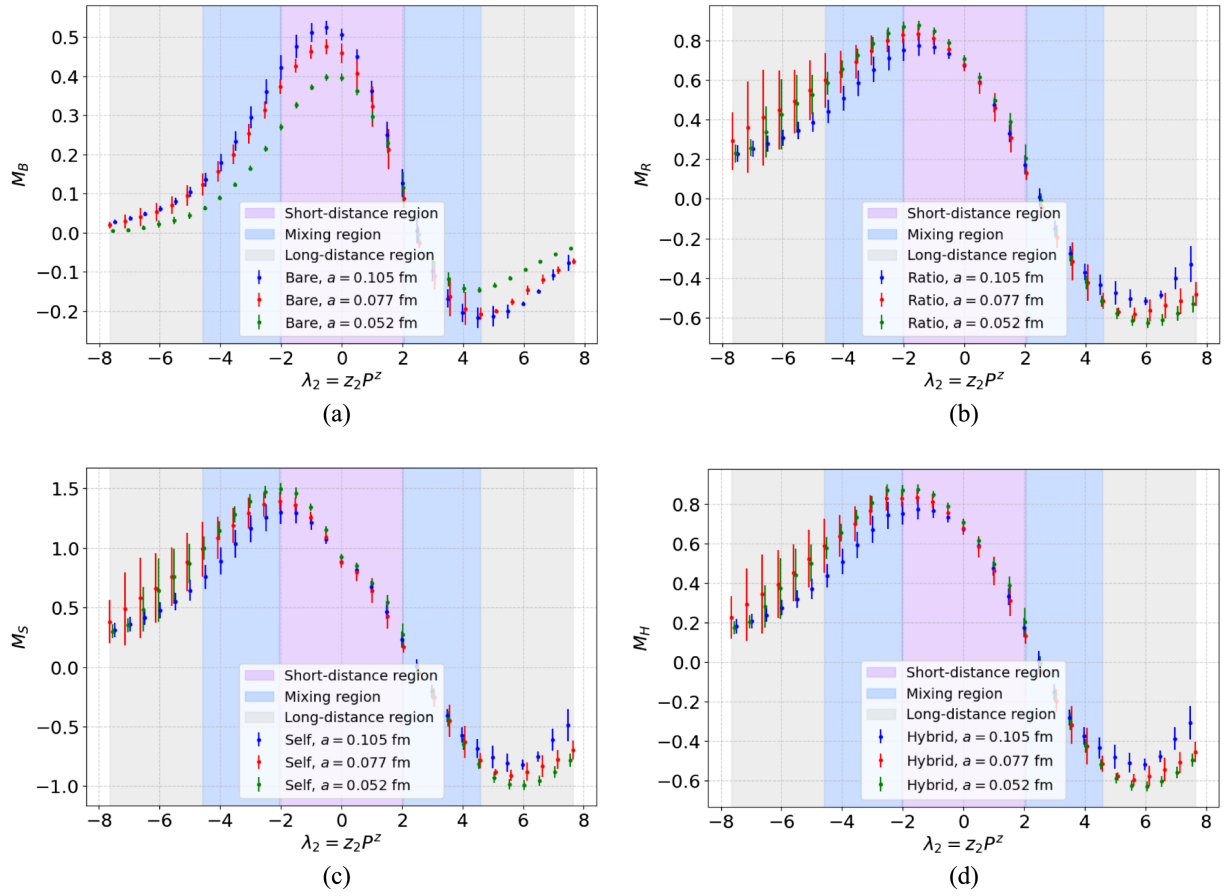

FIG. 14. Bare, ratio scheme, self-renormalized and hybrid renormalization scheme results of the Λ quasi-DA matrix elements at $P^z = 2.0$ GeV, fix $z_1 = 0.250$ fm ($\lambda_1 = 2.522$). (a) Bare result of Λ at $P = 0.2$ GeV. (b) Ratio scheme result of Λ at $P = 0.2$ GeV. (c) Self-renormalized result of Λ at $P = 0.2$ GeV. (d) Hybrid scheme result of Λ at $P = 0.2$ GeV.

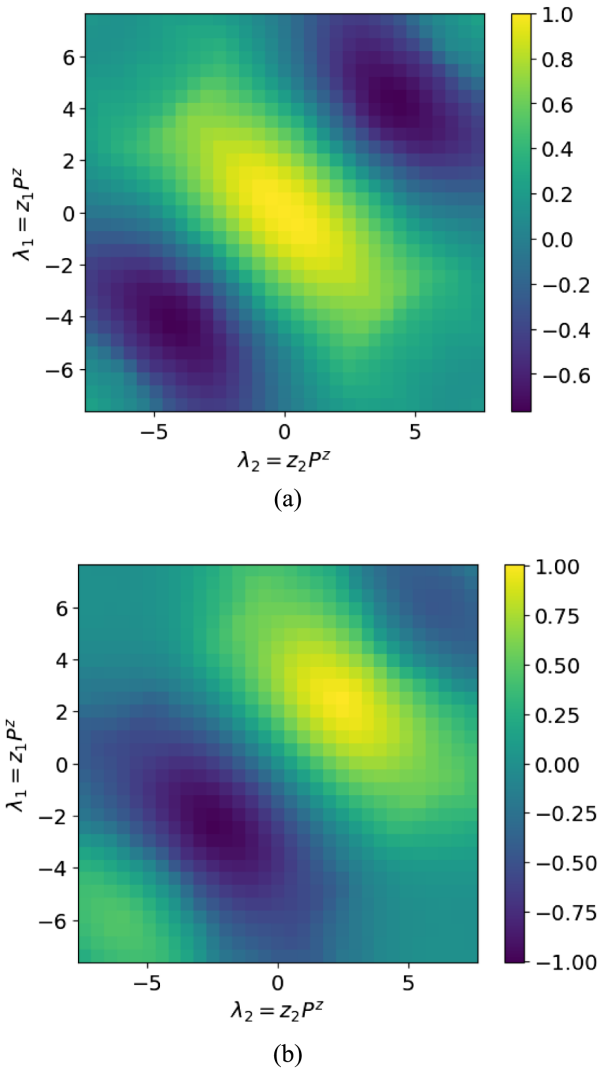

FIG. 15. 2D heatmaps of the hybrid renormalized quasi-DA matrix elements (central values) of the Λ at $P = 2.0$ GeV. (a) Λ, Re, $P = 2.0$ GeV GeV and (b) Λ, Im, $P = 2.0$ GeV GeV.

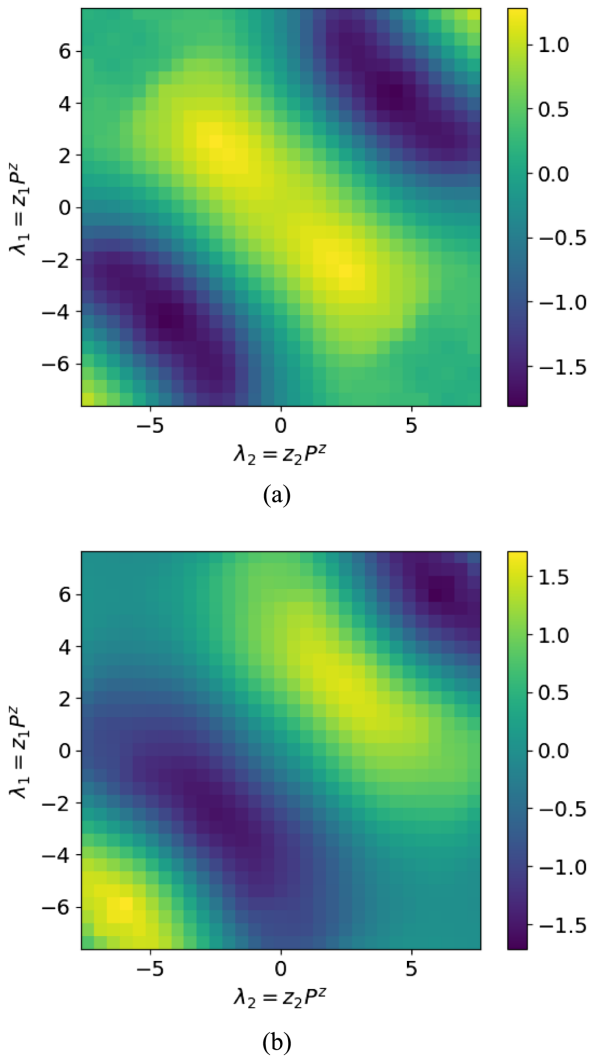

FIG. 16. 2D heatmaps of the hybrid renormalized quasi-DA matrix elements (central values) of the proton at $P = 2.0$ GeV. (a) Proton, Re, $P = 2.0$ GeV GeV and (b) proton, Im, $P = 2.0$ GeV GeV.

pronounced oscillatory behavior across all quadrants, consistent with the expected coordinate space structure of baryon quasi-DAs.

VI. SUMMARY

In this work, we numerically implement the hybrid renormalization scheme based on self-renormalization for the leading-twist A-term of the Λ quasi-DAs and the V/T-terms of the proton quasi-DAs. The linear divergence is extracted by analyzing zero-momentum matrix elements at multiple lattice spacings, $a = \{0.105, 0.077, 0.052\}$ fm. The residual self-renormalization factors are then determined by matching to perturbative matrix elements in the $\overline{\text{MS}}$ scheme. To suppress instabilities caused by the peaked structure in the self-renormalization scheme, we adopt the hybrid renormalization scheme, which combines the ratio scheme at short distances with the self-renormalization at large distances. Finally, we present the renormalized quasi-DAs at both a small momentum of 0.5 GeV and a large momentum of 2.0 GeV.

The renormalized results indicate that the linear divergence associated with the Wilson line self-energy exhibits negligible dependence on the external state, as expected. Moreover, renormalized quasi-DAs show good convergence with respect to lattice spacing, consistent with the expected behavior of residual discretization effects at large P^z. This confirms that the hybrid renormalization scheme results in a reliable continuum limit. Additionally, by properly renormalizing all divergences, the hybrid renormalization scheme yields smooth and continuous quasi-DAs, significantly reducing the complexity of the subsequent Fourier transform and effective matching procedures.

Therefore, this work provides an important and reliable foundation for the precise and systematically correct

computation of baryon LCDAs within the LaMET framework. Building upon the robust renormalization procedure established here, the next goal is to obtain reliable baryon LCDAs in the continuum limit.

The LQCD simulations were performed using the PyQUDA software suite [138] and QUDA [139–141] through HIP programming model [142].

ACKNOWLEDGMENTS

We thank Fusheng Yu, Jiajie Han, and Yuelong Shen for useful discussions. We thank the CLQCD Collaborations for providing us the gauge configurations with dynamical fermions [124], which are generated on the HPC Cluster of ITP-CAS, the Southern Nuclear Science Computing Center (SNSC), the Siyuan-1 cluster supported by the Center for High Performance Computing at Shanghai Jiao Tong University and the Dongjiang Yuan Intelligent Computing Center. This work is supported in part by Natural Science Foundation of China under Grants No. 12205106, No. 12575084, No. 12125503, No. 12305103, No. 12375080, No. 12375069, No. 12293060, No. 12293062, No. 12435002, No. 12447101, No. 12175073, No. 12275277, No. 12435004, and No. 12222503. Y. B. Y. is supported in part by the National Key R&D Program of China No. 2024YFE0109800, and by the Strategic Priority Research Program of Chinese Academy of Sciences, Grant No. YSBR-101. J. H. Z. is supported in part by the Ministry of Science and Technology of China under Grant No. 2024YFA1611004, and by CUHK-Shenzhen under Grant No. UDF01002851. Q. A. Z. is supported in part by the Fundamental Research Funds for the Central Universities. J. H is supported by Guangdong Major Project of Basic and Applied Basic Research No. 2025A1515012199. The computations in this paper were run on the Siyuan-1 cluster supported by the Center for High Performance Computing at Shanghai Jiao Tong University, and Advanced Computing East China Subcenter.

DATA AVAILABILITY

The data that support the findings of this article are not publicly available upon publication because it is not technically feasible and/or the cost of preparing, depositing, and hosting the data would be prohibitive within the terms of this research project. The data are available from the authors upon reasonable request.

APPENDIX A: SYMMETRY IN BARYON DISTRIBUTIONS

In lattice QCD calculations, it is often useful to exploit symmetry relations derived from theoretical considerations to check the correctness and consistency of numerical results. Since the proton is an isospin-$\frac{1}{2}$ state, the following identity holds:

$$\left\langle 0\left|\left(T^2-\frac{1}{2}\left(\frac{1}{2}+1\right)\right)(\varepsilon^{ijk}u^i_\alpha(1)u^j_\beta(2)d^k_\gamma(3))\right|P\right\rangle=0, \tag{A1}$$

where

$$T^2=\frac{1}{2}(T_+T_-+T_-T_+)+T_3^2 \tag{A2}$$

is the quadratic Casimir operator of the isospin $\mathfrak{su}(2)$ algebra in the adjoint representation. This condition leads to the constraint [143],

$$\begin{aligned}&\langle 0|\varepsilon^{ijk}u^i_\alpha(1)u^j_\beta(2)d^k_\gamma(3)|P\rangle+\langle 0|\varepsilon^{ijk}u^i_\alpha(1)u^j_\gamma(3)d^k_\beta(2)|P\rangle\\&\quad+\langle 0|\varepsilon^{ijk}u^i_\gamma(3)u^j_\beta(2)d^k_\alpha(1)|P\rangle=0.\end{aligned} \tag{A3}$$

To bring all terms into the same spinor index order (α,β,γ), one can employ the following Fierz identities [143],

$$\begin{aligned}(v_1)_{\gamma\beta,\alpha}&=\frac{1}{2}(v_1-a_1-t_1)_{\alpha\beta,\gamma},\\(a_1)_{\gamma\beta,\alpha}&=\frac{1}{2}(-v_1+a_1-t_1)_{\alpha\beta,\gamma},\\(t_1)_{\gamma\beta,\alpha}&=-(v_1+a_1)_{\alpha\beta,\gamma},\end{aligned} \tag{A4}$$

where the Lorentz structures are defined as

$$\begin{aligned}(v_1)_{\alpha\beta,\gamma}&=(\not{P}C)_{\alpha\beta}(\gamma_5N)_\gamma,(a_1)_{\alpha\beta,\gamma}\\&=(\not{P}\gamma_5C)_{\alpha\beta}(N)_\gamma,(t_1)_{\alpha\beta,\gamma}\\&=(P^\nu i\sigma_{\mu\nu}C)_{\alpha\beta}(\gamma^\mu\gamma_5N)_\gamma.\end{aligned}$$

Applying this decomposition to Eq. (A3), one arrives at the following identity:

$$\begin{aligned}0=&[2T(x_1,x_2,x_3)-V(x_1,x_3,x_2)+A(x_1,x_3,x_2)-V(x_3,x_2,x_1)-A(x_3,x_2,x_1)](t_1)_{\alpha\beta,\gamma}\\&+[2V(x_1,x_2,x_3)+2V(x_1,x_3,x_2)+2A(x_1,x_3,x_2)-2T(x_1,x_3,x_2)+V(x_3,x_2,x_1)-A(x_3,x_2,x_1)\\&-2T(x_3,x_2,x_1)](v_1)_{\alpha\beta,\gamma}+[2A(x_1,x_2,x_3)+2V(x_1,x_3,x_2)+2A(x_1,x_3,x_2)+2T(x_1,x_3,x_2)-V(x_3,x_2,x_1)\\&+A(x_3,x_2,x_1)-2T(x_3,x_2,x_1)](a_1)_{\alpha\beta,\gamma}.\end{aligned} \tag{A5}$$

By making use of the known symmetry properties of the functions V, A, and T, this equation reduces to a single nontrivial constraint. For baryons not of the Λ type, this leads to the well-known relation [30],

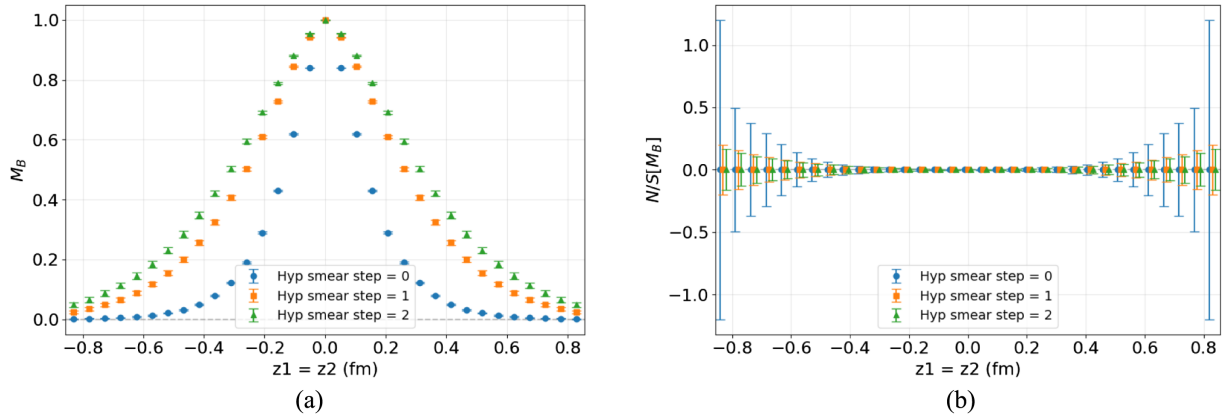

FIG. 17. Zero-momentum quasi-DA and its corresponding noise-to-signal ratio for the Λ (A-term) along $z_1 = z_2$, for H48P32 ($a = 0.052$ fm), with HYP smearing iterations $n_{\mathrm{HYP}} = 0$ (blue), 1 (orange), and 2 (green). (a) Bare quasi-DA, Λ, $P = 0$ and (b) Noise-to-signal ratio, Λ, $P = 0$.

$$2T(x_1,x_2,x_3) = (V-A)(x_1,x_3,x_2) + (V-A)(x_2,x_3,x_1). \tag{A6}$$

For the Λ baryon, the corresponding relation becomes

$$2T(x_1,x_2,x_3) = (V-A)(x_1,x_3,x_2) - (V-A)(x_2,x_3,x_1). \tag{A7}$$

Besides, in some lattice implementations, the order of valence quarks in the interpolating operator may be changed to simplify the contraction structure. For example, the flavor ordering *udu* may be used for the proton instead of the canonical *uud*. In such cases, the Fierz identities in Eq. (A4) can be used to relate the LCDA defined in the new flavor ordering to those defined in the standard basis.

APPENDIX B: DETAILS FOR HYP SMEARING

1. Improvement of the signal

HYP smearing [133,134] is a gauge-field processing technique that applies weighted averaging of adjacent gauge links to obtain smoother gauge configurations. In our calculation of baryon quasi-DAs with nonlocal shifts, replacing the gauge links between quark fields with HYP-smeared links can significantly improve the signal-to-noise ratio of nonlocal matrix element.

Figure 17(a) displays the zero-momentum quasi-DA for the Λ (A-term) along the $z_1 = z_2$ direction with HYP smearing iterations $n_{\mathrm{HYP}} = 0$, 1, 2, and the subfigure (b) shows the corresponding noise-to-signal ratios. With single-step HYP smearing, the statistical errors at large distances decrease considerably, while a second smearing step provides marginal additional improvement. Therefore, we choose single-step HYP smearing in our lattice simulation.

Further more, Fig. 18 shows the effective mass of the Λ baryon matrix element at a specific nonlocal point ($z_1 = 6a, z_2 = 0$) using both original and HYP-smeared gauge links, for momenta $P^z = 0$ GeV and $P^z = 1.49$ GeV. The use of HYP-smeared links substantially reduces the statistical uncertainties, while the effective mass behavior remains consistent across different momenta. This indicates that smearing the sink-side gauge links does not alter the excited-state contamination.

2. Impact on linear divergence

HYP smearing smooths the short-distance behavior of gauge links, including the modification of the linear divergence. However, this modification does not affect the renormalized physical results in the ratio or self-renormalization schemes. The parametric form of self-renormalization remains valid for smeared results, as established in Ref. [53].

To ensure that HYP smearing does not affect the physical results, we also performed a simple check using the ratio scheme renormalization. Figure 19(a) displays the bare

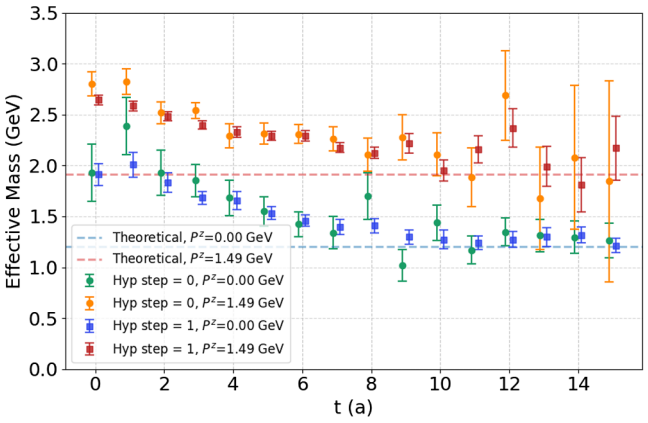

FIG. 18. Effective mass plots for the Λ at a nonlocal point ($z_1 = 0.36$ fm, $z_2 = 0$) with original and HYP-smeared gauge links, for H48P32 ($a = 0.052$ fm), with $P^z = 0$ GeV and $P^z = 1.49$ GeV.

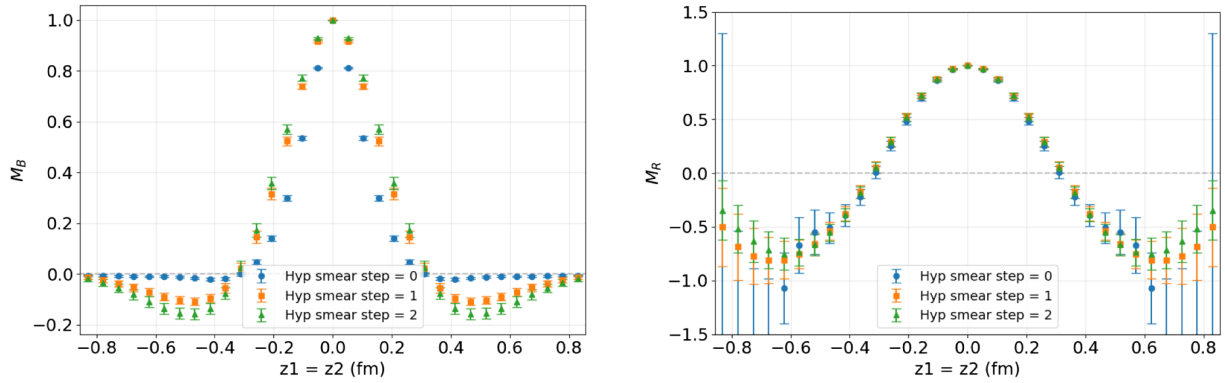

FIG. 19. Bare quasi-DA and ratio-scheme results for the Λ (A-term) at $P^z = 1.49$ GeV along $z_1 = z_2$, for H48P32 ($a = 0.052$ fm), with HYP smearing iterations $n_{\mathrm{HYP}} = 0$ (blue), 1 (orange), and 2 (green). (a) Bare quasi-DA, Λ, $P = 1.49$ GeV and (b) Ratio scheme quasi-DA, Λ, $P = 1.49$ GeV.

quasi-DA for the Λ (A-term) at $P^z = 1.49$ GeV with $n_{\mathrm{HYP}} = 0$, 1, 2, while Fig. 19(b) shows the corresponding ratio scheme quasi-DA results (renormalized by the zero-momentum matrix elements). Within uncertainties, the renormalized quasi-DAs remain consistent across different smearing levels, confirming that the ultraviolet

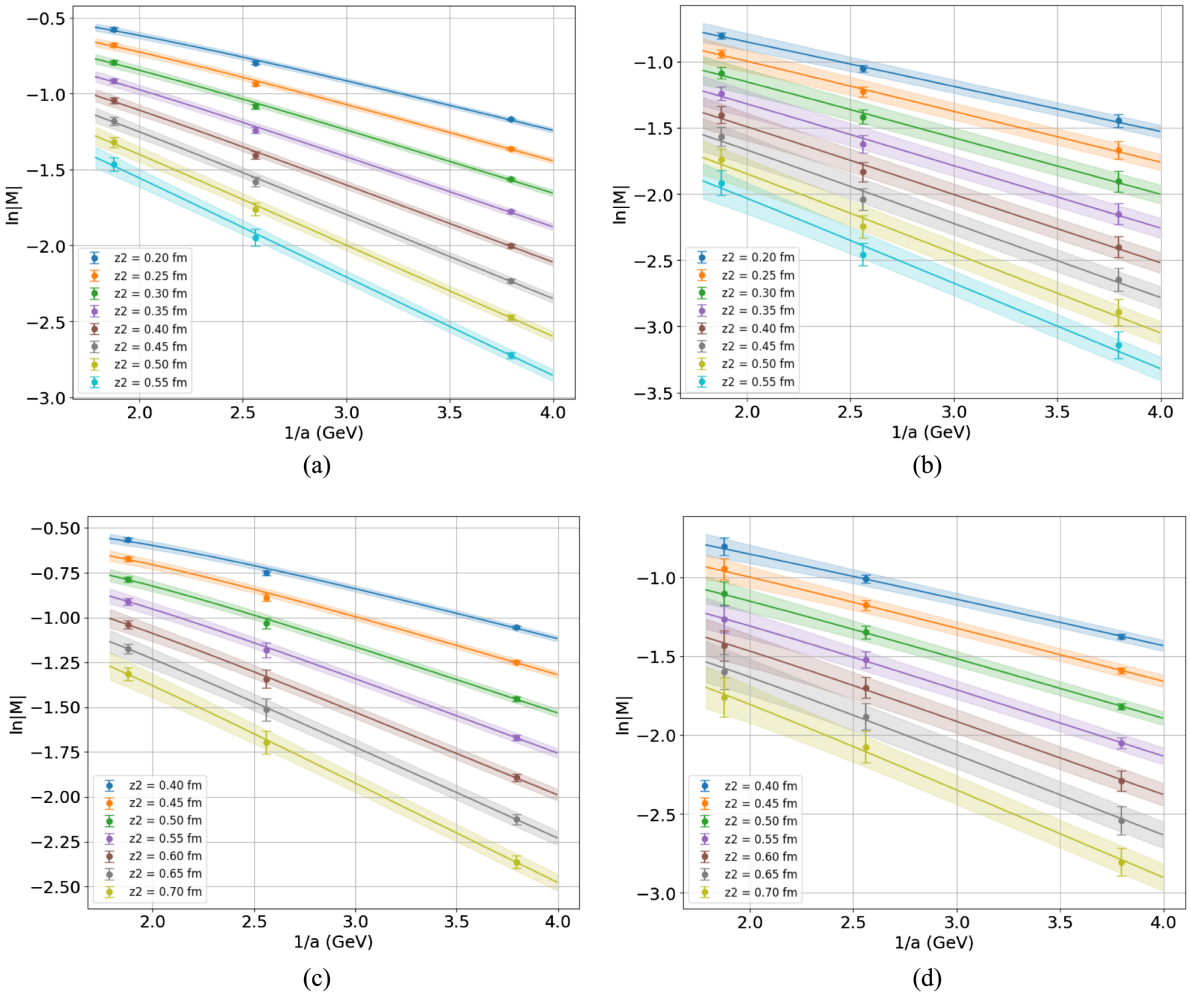

FIG. 20. Extraction of the linear divergence with lattice spacing dependence for zero-momentum matrix elements of the proton and the Λ. (a) Λ, $z_1 = -0.25$ fm. (b) Proton, $z_1 = -0.25$ fm. (c) Λ, $z_1 = 0.20$ fm. (b) Proton, $z_1 = 0.20$ fm.

divergences introduced by HYP smearing are mainly linear divergence and can be fully removed by renormalization.

APPENDIX C: LINEAR DIVERGENCES IN THE Λ AND THE PROTON LCDAS

To illustrate the clear linear dependence on lattice spacings for both the Λ and the proton, we show more matrix elements plotted against 1/a using a logarithmic scale in Fig. 20.

Theoretically, the linear divergence dominated by the lattice gauge field should be independent of the external states. This can be verified by comparing the ratios of bare quasi-DA matrix elements for the proton (V-term) and the Λ (A-term) across three ensembles. As shown in Fig. 21, we present the ratio results for both $P^z = 0$ and $P^z = 0.5$ GeV cases on three ensembles. It can be observed that the ratios are consistent within uncertainties for three different lattice spacings. Consequently, these linear divergences largely cancel out in the ratio, with only minor discrepancies appearing in the short-distance region, suggesting that the linear divergence indeed does not depend on the external states.

APPENDIX D: MORE RESULTS OF BARYON QUASI-DAS USING DIFFERENT SCHEMES

More cases for the Λ (A-term) and the proton (V-term) quasi-DAs in different schemes are shown in this section from Figs. 22–45.

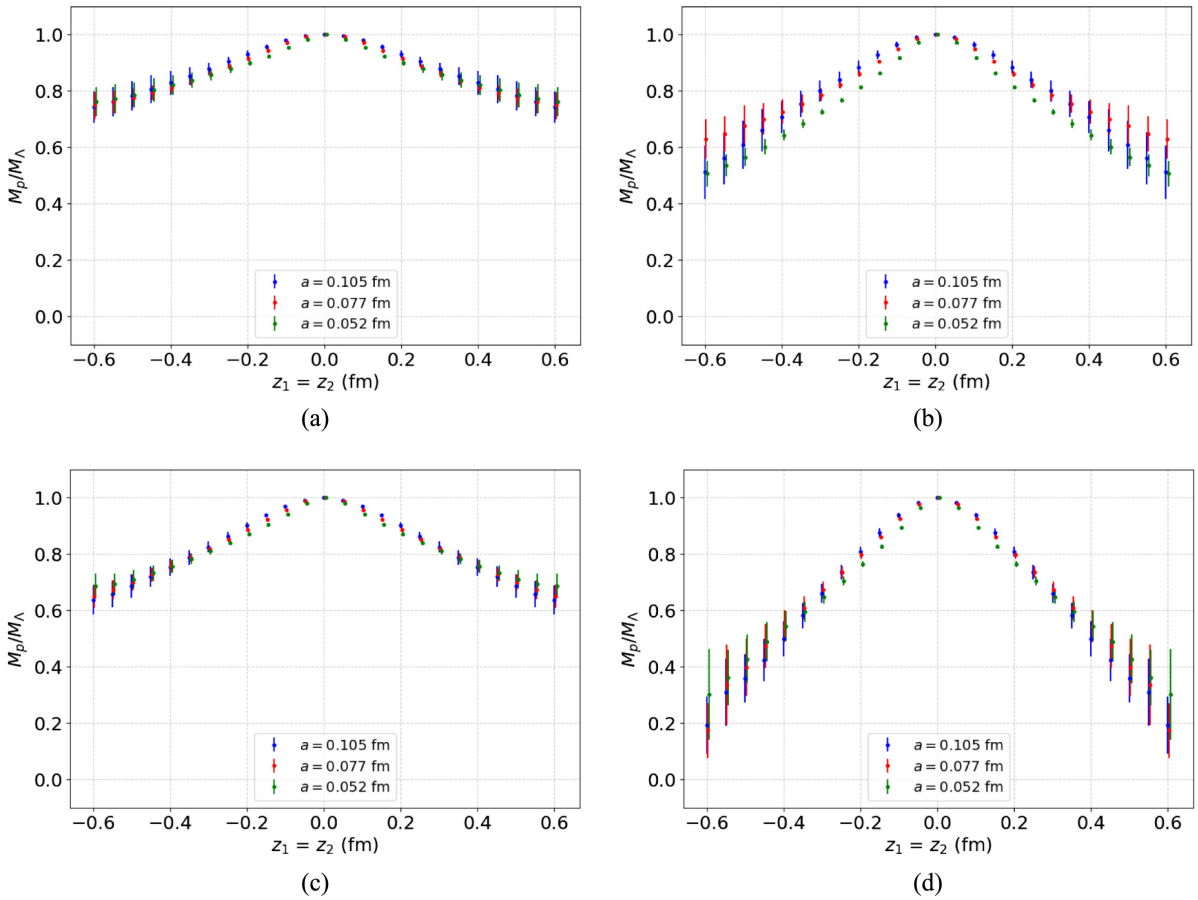

FIG. 21. Ratio of the proton (V-term) quasi-DA to the Λ (A-term) quasi-DA on different lattice spacings and momenta. (a) $z_1 = 0$, $P^z = 0$. (b) $z_1 = z_2$, $P^z = 0$. (c) $z_1 = 0$, $P^z = 0.5$ GeV. (d) $z_1 = z_2$, $P^z = 0.5$ GeV.

1. More results of the Λ (A-term) quasi-DA at $P^z = 0.5$ GeV in different schemes

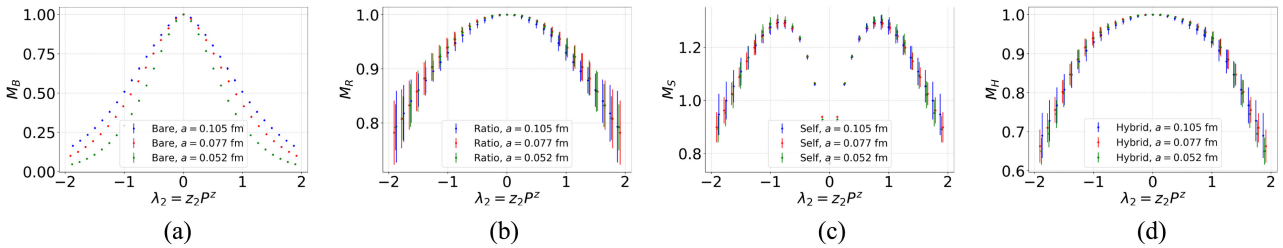

FIG. 22. Results of the Λ quasi-DA matrix elements in different schemes and with $P^z = 0.5$ GeV, $z_1 = 0.000$ fm. (a) Bare result of Λ at $P = 0.5$ GeV. (b) Ratio scheme result of Λ at $P = 0.5$ GeV. (c) Self-scheme result of Λ at $P = 0.5$ GeV. (d) Hybrid scheme result of Λ at $P = 0.5$ GeV.

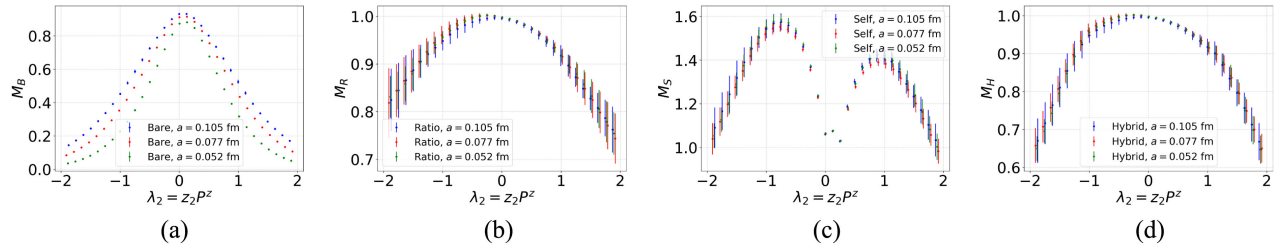

FIG. 23. Results of the Λ quasi-DA matrix elements in different schemes and with $P^z = 0.5$ GeV, $z_1 = 0.100$ fm. (a) Bare result of Λ at $P = 0.5$ GeV. (b) Ratio scheme result of Λ at $P = 0.5$ GeV. (c) Self-scheme result of Λ at $P = 0.5$ GeV. (d) Hybrid scheme result of Λ at $P = 0.5$ GeV.

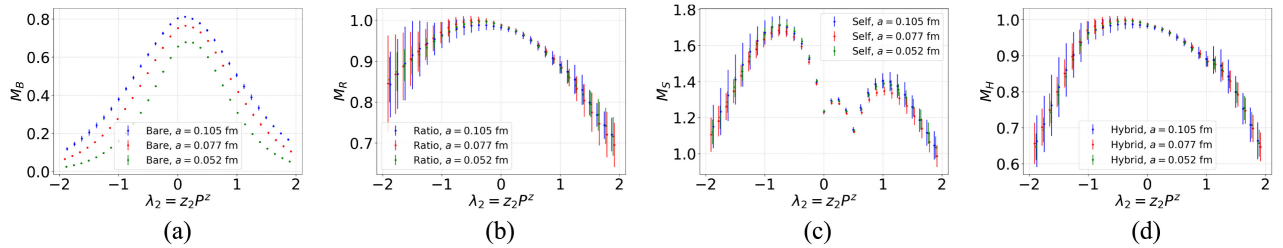

FIG. 24. Results of the Λ quasi-DA matrix elements in different schemes and with $P^z = 0.5$ GeV, $z_1 = 0.200$ fm. (a) Bare result of Λ at $P = 0.5$ GeV. (b) Ratio scheme result of Λ at $P = 0.5$ GeV. (c) Self-scheme result of Λ at $P = 0.5$ GeV. (d) Hybrid scheme result of Λ at $P = 0.5$ GeV.

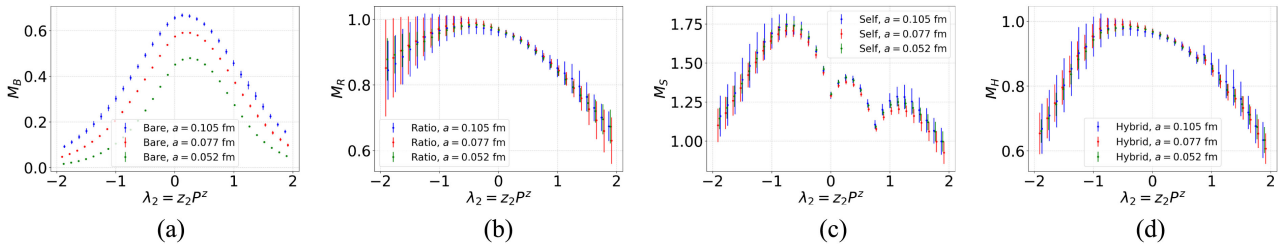

FIG. 25. Results of the Λ quasi-DA matrix elements in different schemes and with $P^z = 0.5$ GeV, $z_1 = 0.300$ fm. (a) Bare result of Λ at $P = 0.5$ GeV. (b) Ratio scheme result of Λ at $P = 0.5$ GeV. (c) Self-scheme result of Λ at $P = 0.5$ GeV. (d) Hybrid scheme result of Λ at $P = 0.5$ GeV.

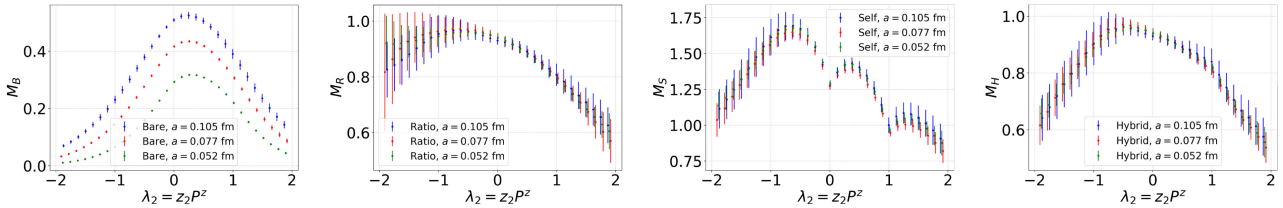

FIG. 26. Results of the Λ quasi-DA matrix elements in different schemes and with $P^z = 0.5$ GeV, $z_1 = 0.400$ fm. (a) Bare result of Λ at $P = 0.5$ GeV. (b) Ratio scheme result of Λ at $P = 0.5$ GeV. (c) Self-scheme result of Λ at $P = 0.5$ GeV. (d) Hybrid scheme result of Λ at $P = 0.5$ GeV.

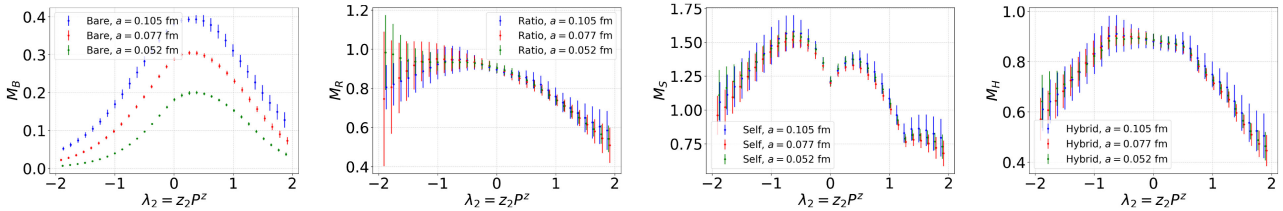

FIG. 27. Results of the Λ quasi-DA matrix elements in different schemes and with $P^z = 0.5$ GeV, $z_1 = 0.500$ fm. (a) Bare result of Λ at $P = 0.5$ GeV. (b) Ratio scheme result of Λ at $P = 0.5$ GeV. (c) Self-scheme result of Λ at $P = 0.5$ GeV. (d) Hybrid scheme result of Λ at $P = 0.5$ GeV.

2. More results of the Λ (A-term) quasi-DA at $P^z = 2.0$ GeV in different schemes

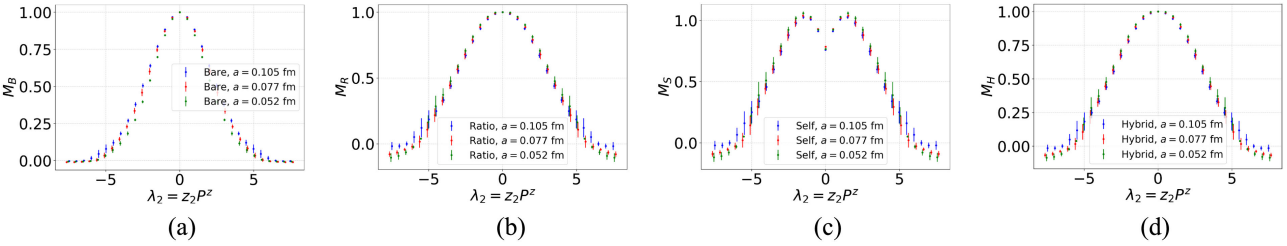

FIG. 28. Results of the Λ quasi-DA matrix elements in different schemes and with $P^z = 2.0$ GeV, $z_1 = 0.000$ fm. (a) Bare result of Λ at $P = 2.0$ GeV. (b) Ratio scheme result of Λ at $P = 2.0$ GeV. (c) Self-scheme result of Λ at $P = 2.0$ GeV. (d) Hybrid scheme result of Λ at $P = 2.0$ GeV.

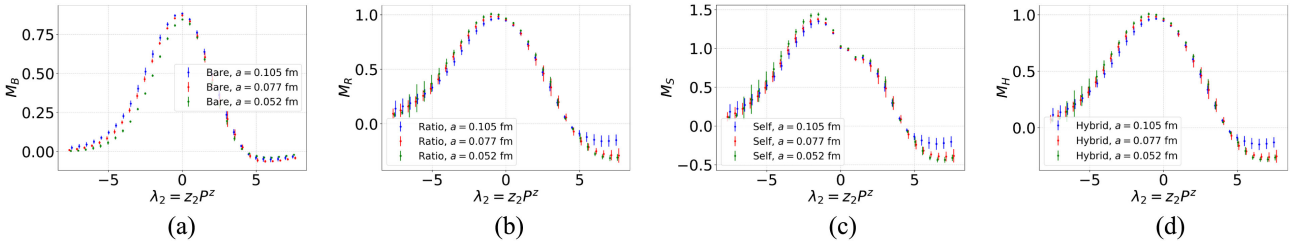

FIG. 29. Results of the Λ quasi-DA matrix elements in different schemes and with $P^z = 2.0$ GeV, $z_1 = 0.100$ fm. (a) Bare result of Λ at $P = 2.0$ GeV. (b) Ratio scheme result of Λ at $P = 2.0$ GeV. (c) Self-scheme result of Λ at $P = 2.0$ GeV. (d) Hybrid scheme result of Λ at $P = 2.0$ GeV.

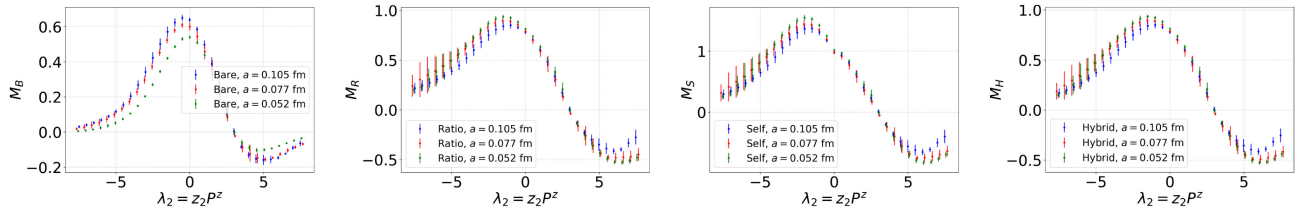

FIG. 30. Results of the Λ quasi-DA matrix elements in different schemes and with $P^z = 2.0$ GeV, $z_1 = 0.200$ fm. (a) Bare result of Λ at $P = 2.0$ GeV. (b) Ratio scheme result of Λ at $P = 2.0$ GeV. (c) Self-scheme result of Λ at $P = 2.0$ GeV. (d) Hybrid scheme result of Λ at $P = 2.0$ GeV.

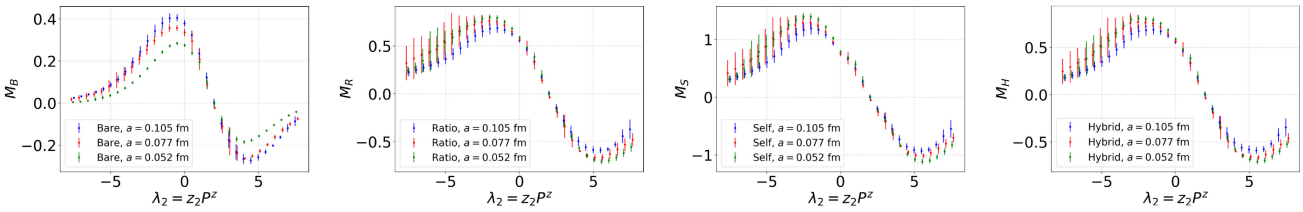

FIG. 31. Results of the Λ quasi-DA matrix elements in different schemes and with $P^z = 2.0$ GeV, $z_1 = 0.300$ fm. (a) Bare result of Λ at $P = 2.0$ GeV. (b) Ratio scheme result of Λ at $P = 2.0$ GeV. (c) Self-scheme result of Λ at $P = 2.0$ GeV. (d) Hybrid scheme result of Λ at $P = 2.0$ GeV.

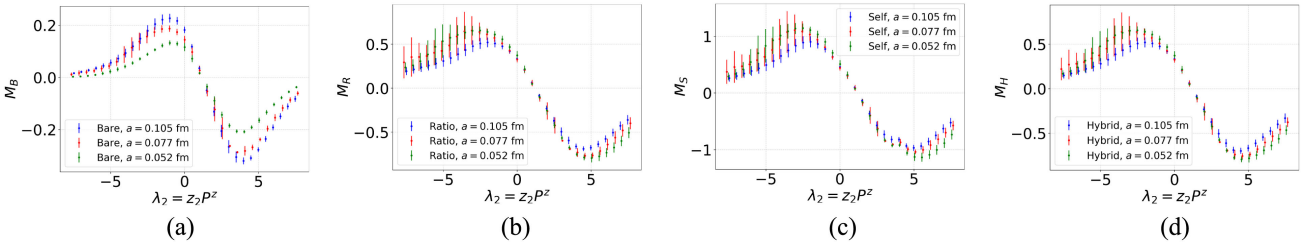

FIG. 32. Results of the Λ quasi-DA matrix elements in different schemes and with $P^z = 2.0$ GeV, $z_1 = 0.400$ fm. (a) Bare result of Λ at $P = 2.0$ GeV. (b) Ratio scheme result of Λ at $P = 2.0$ GeV. (c) Self-scheme result of Λ at $P = 2.0$ GeV. (d) Hybrid scheme result of Λ at $P = 2.0$ GeV.

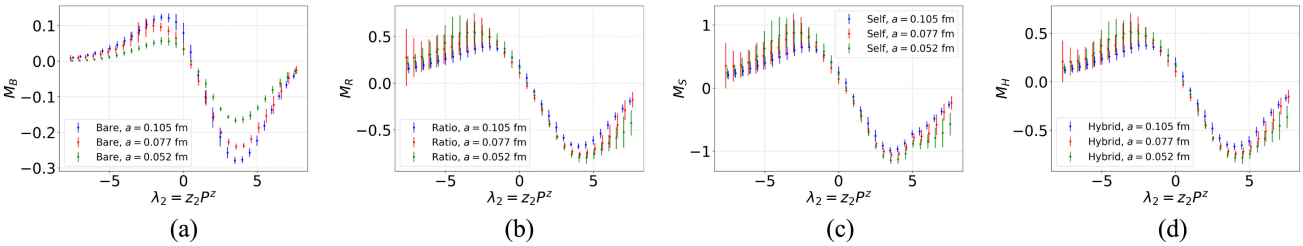

FIG. 33. Results of the Λ quasi-DA matrix elements in different schemes and with $P^z = 2.0$ GeV, $z_1 = 0.500$ fm. (a) Bare result of Λ at $P = 2.0$ GeV. (b) Ratio scheme result of Λ at $P = 2.0$ GeV. (c) Self-scheme result of Λ at $P = 2.0$ GeV. (d) Hybrid scheme result of Λ at $P = 2.0$ GeV.

3. More results of the proton (V-term) quasi-DA at $P^z = 0.5$ GeV in different schemes

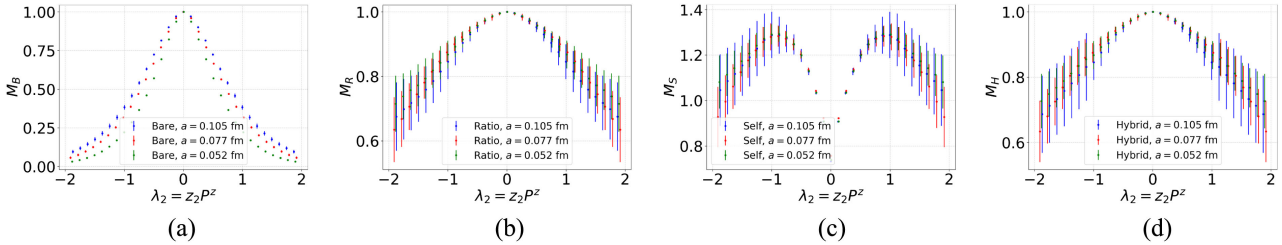

FIG. 34. Results of the proton quasi-DA matrix elements in different schemes and with $P^z = 0.5$ GeV, $z_1 = 0.000$ fm. (a) Bare result of proton at $P = 0.5$ GeV. (b) Ratio scheme result of proton at $P = 0.5$ GeV. (c) Self-scheme result of proton at $P = 0.5$ GeV. (d) Hybrid scheme result of proton at $P = 0.5$ GeV.

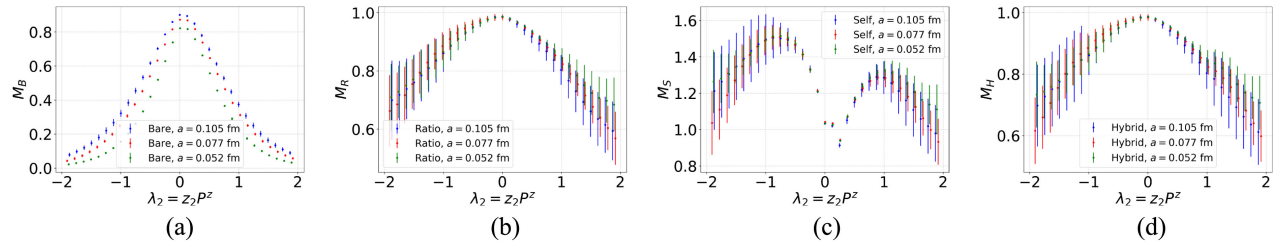

FIG. 35. Results of the proton quasi-DA matrix elements in different schemes and with $P^z = 0.5$ GeV, $z_1 = 0.100$ fm. (a) Bare result of proton at $P = 0.5$ GeV. (b) Ratio scheme result of proton at $P = 0.5$ GeV. (c) Self-scheme result of proton at $P = 0.5$ GeV. (d) Hybrid scheme result of proton at $P = 0.5$ GeV.

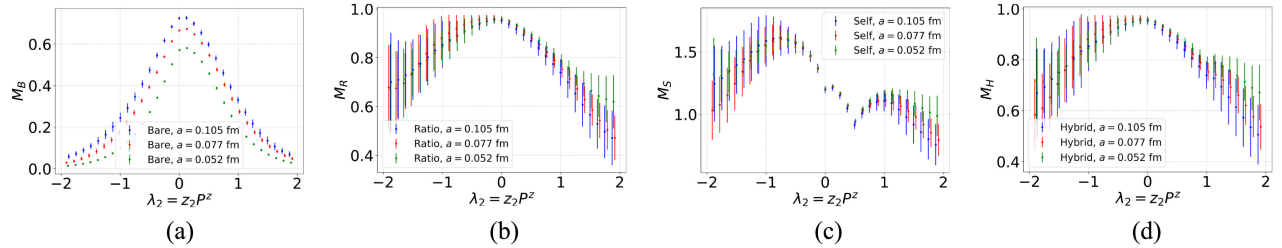

FIG. 36. Results of the proton quasi-DA matrix elements in different schemes and with $P^z = 0.5$ GeV, $z_1 = 0.200$ fm. (a) Bare result of proton at $P = 0.5$ GeV. (b) Ratio scheme result of proton at $P = 0.5$ GeV. (c) Self-scheme result of proton at $P = 0.5$ GeV. (d) Hybrid scheme result of proton at $P = 0.5$ GeV.

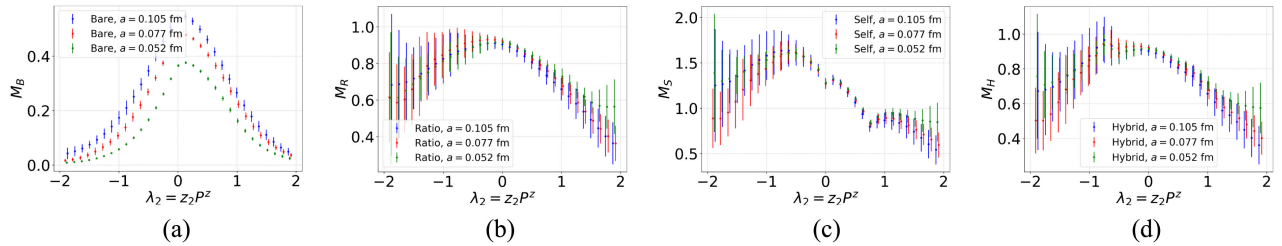

FIG. 37. Results of the proton quasi-DA matrix elements in different schemes and with $P^z = 0.5$ GeV, $z_1 = 0.300$ fm. (a) Bare result of proton at $P = 0.5$ GeV. (b) Ratio scheme result of proton at $P = 0.5$ GeV. (c) Self-scheme result of proton at $P = 0.5$ GeV. (d) Hybrid scheme result of proton at $P = 0.5$ GeV.

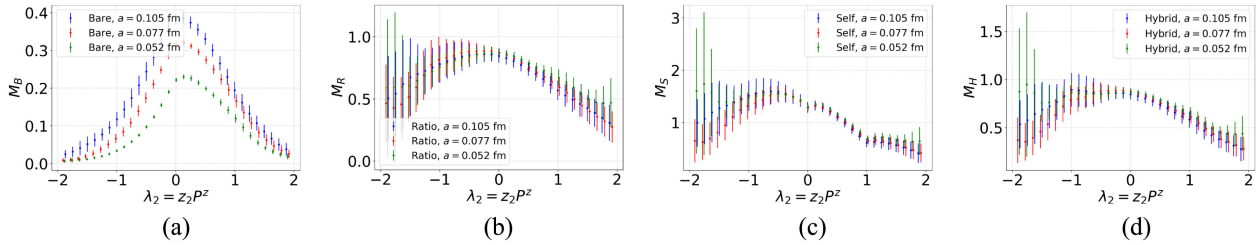

FIG. 38. Results of the proton quasi-DA matrix elements in different schemes and with $P^z = 0.5$ GeV, $z_1 = 0.400$ fm. (a) Bare result of proton at $P = 0.5$ GeV. (b) Ratio scheme result of proton at $P = 0.5$ GeV. (c) Self-scheme result of proton at $P = 0.5$ GeV. (d) Hybrid scheme result of proton at $P = 0.5$ GeV.

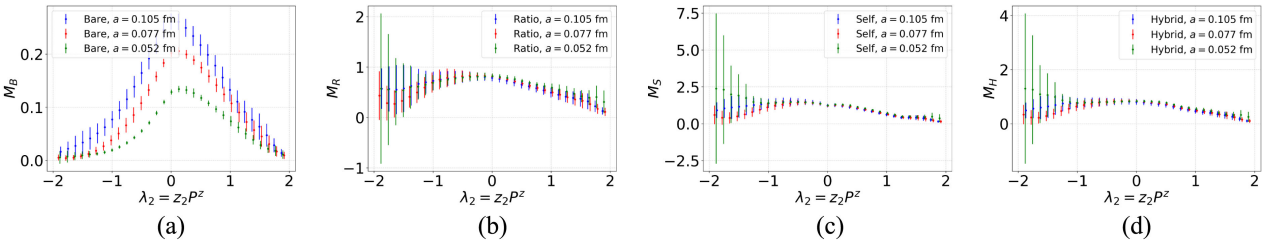

FIG. 39. Results of the proton quasi-DA matrix elements in different schemes and with $P^z = 0.5$ GeV, $z_1 = 0.500$ fm. (a) Bare result of proton at $P = 0.5$ GeV. (b) Ratio scheme result of proton at $P = 0.5$ GeV. (c) Self-scheme result of proton at $P = 0.5$ GeV. (d) Hybrid scheme result of proton at $P = 0.5$ GeV.

4. More results of the proton (V-term) quasi-DA at $P^z = 2.0$ GeV in different schemes

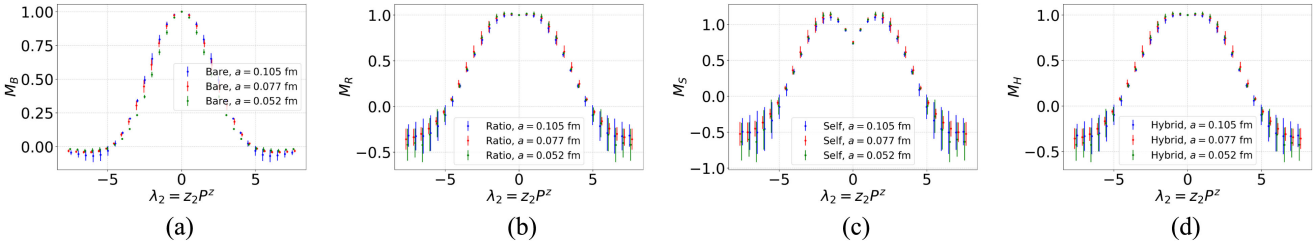

FIG. 40. Results of the proton quasi-DA matrix elements in different schemes and with $P^z = 2.0$ GeV, $z_1 = 0.000$ fm. (a) Bare result of proton at $P = 2.0$ GeV. (b) Ratio scheme result of proton at $P = 2.0$ GeV. (c) Self-scheme result of proton at $P = 2.0$ GeV. (d) Hybrid scheme result of proton at $P = 2.0$ GeV.

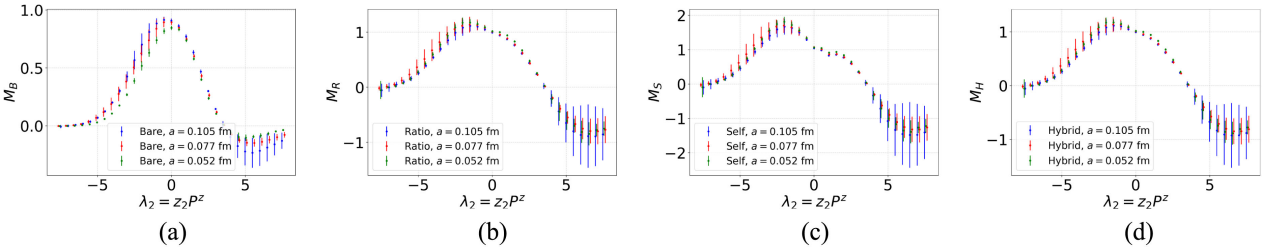

FIG. 41. Results of the proton quasi-DA matrix elements in different schemes and with $P^z = 2.0$ GeV, $z_1 = 0.100$ fm. (a) Bare result of proton at $P = 2.0$ GeV. (b) Ratio scheme result of proton at $P = 2.0$ GeV. (c) Self-scheme result of proton at $P = 2.0$ GeV. (d) Hybrid scheme result of proton at $P = 2.0$ GeV.

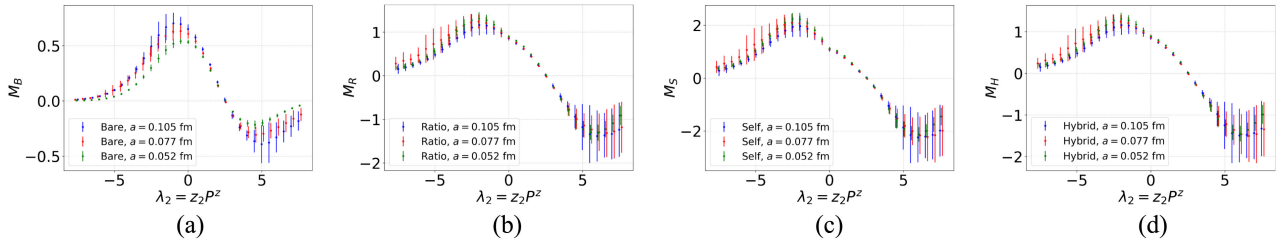

FIG. 42. Results of the proton quasi-DA matrix elements in different schemes and with $P^z = 2.0$ GeV, $z_1 = 0.200$ fm. (a) Bare result of proton at $P = 2.0$ GeV. (b) Ratio scheme result of proton at $P = 2.0$ GeV. (c) Self-scheme result of proton at $P = 2.0$ GeV. (d) Hybrid scheme result of proton at $P = 2.0$ GeV.

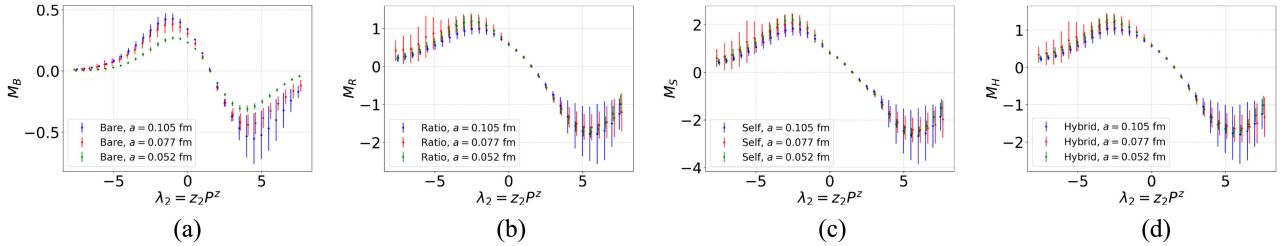

FIG. 43. Results of the proton quasi-DA matrix elements in different schemes and with $P^z = 2.0$ GeV, $z_1 = 0.300$ fm. (a) Bare result of proton at $P = 2.0$ GeV. (b) Ratio scheme result of proton at $P = 2.0$ GeV. (c) Self-scheme result of proton at $P = 2.0$ GeV. (d) Hybrid scheme result of proton at $P = 2.0$ GeV.

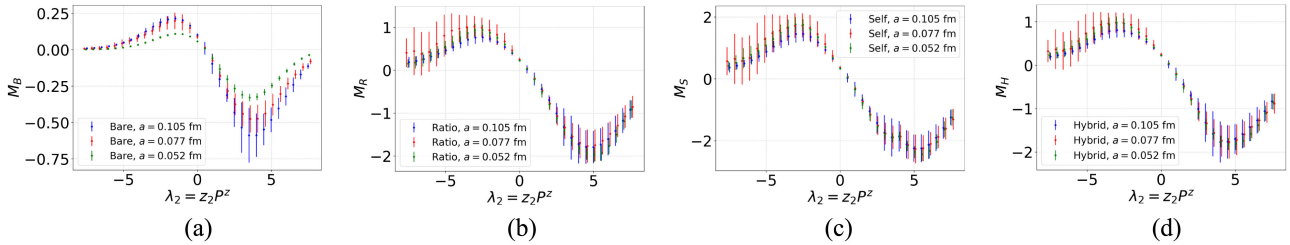

FIG. 44. Results of the proton quasi-DA matrix elements in different schemes and with $P^z = 2.0$ GeV, $z_1 = 0.400$ fm. (a) Bare result of proton at $P = 2.0$ GeV. (b) Ratio scheme result of proton at $P = 2.0$ GeV. (c) Self-scheme result of proton at $P = 2.0$ GeV. (d) Hybrid scheme result of proton at $P = 2.0$ GeV.

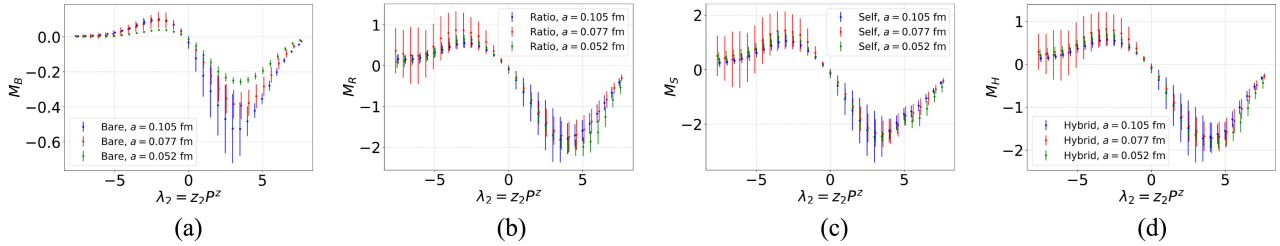

FIG. 45. Results of the proton quasi-DA matrix elements in different schemes and with $P^z = 2.0$ GeV, $z_1 = 0.500$ fm. (a) Bare result of proton at $P = 2.0$ GeV. (b) Ratio scheme result of proton at $P = 2.0$ GeV. (c) Self-scheme result of proton at $P = 2.0$ GeV. (d) Hybrid scheme result of proton at $P = 2.0$ GeV.

[1] R. Aaij *et al.* (LHCb Collaboration), Nature (London) **643**, 1223 (2025).
[2] R. Aaij *et al.* (LHCb Collaboration), Phys. Rev. Lett. **134**, 101802 (2025).
[3] Y.-M. Wang and Y.-L. Shen, J. High Energy Phys. 02 (2016) 179.
[4] J.-J. Han, Y. Li, H.-n. Li, Y.-L. Shen, Z.-J. Xiao, and F.-S. Yu, Eur. Phys. J. C **82**, 686 (2022).
[5] K.-S. Huang, W. Liu, Y.-L. Shen, and F.-S. Yu, Eur. Phys. J. C **83**, 272 (2023).
[6] J.-J. Han, J.-X. Yu, Y. Li, H.-n. Li, J.-P. Wang, Z.-J. Xiao, and F.-S. Yu, Phys. Rev. Lett. **134**, 221801 (2025).
[7] J.-J. Han, J.-X. Yu, Y. Li, H.-n. Li, J.-P. Wang, Z.-J. Xiao, and F.-S. Yu, Phys. Rev. D **112**, 053007 (2025).
[8] L.-S. Lu, C.-D. Lü, Y.-L. Shen, and Y.-B. Wei, J. High Energy Phys. 09 (2025) 172.
[9] W. Wang, Phys. Lett. B **708**, 119 (2012).
[10] L.-B. Chen, W. Chen, F. Feng, S. Hu, and Y. Jia, Phys. Rev. Lett. **135**, 131903 (2025).
[11] G. S. Bali, V. M. Braun, S. Bürger, M. Göckeler, M. Gruber, F. Kaiser, B. A. Kniehl, O. L. Veretin, and P. Wein (RQCD Collaboration), Phys. Rev. D **111**, 094517 (2025).
[12] G. S. Bali, V. M. Braun, M. Göckeler, M. Gruber, F. Hutzler, P. Korcyl, B. Lang, and A. Schäfer (RQCD Collaboration), Phys. Lett. B **774**, 91 (2017).
[13] G. S. Bali, V. M. Braun, S. Bürger, M. Göckeler, M. Gruber, F. Hutzler, P. Korcyl, A. Schäfer, A. Sternbeck, and P. Wein (RQCD Collaboration), J. High Energy Phys. 08 (2019) 065; 11 (2020) 037(E).
[14] J.-H. Zhang, J.-W. Chen, X. Ji, L. Jin, and H.-W. Lin, Phys. Rev. D **95**, 094514 (2017).
[15] J.-H. Zhang, L. Jin, H.-W. Lin, A. Schäfer, P. Sun, Y.-B. Yang, R. Zhang, Y. Zhao, and J.-W. Chen (LP3 Collaboration), Nucl. Phys. **B939**, 429 (2019).
[16] R. Zhang, C. Honkala, H.-W. Lin, and J.-W. Chen, Phys. Rev. D **102**, 094519 (2020).
[17] X. Gao, A. D. Hanlon, N. Karthik, S. Mukherjee, P. Petreczky, P. Scior, S. Syritsyn, and Y. Zhao, Phys. Rev. D **106**, 074505 (2022).
[18] J. Holligan, X. Ji, H.-W. Lin, Y. Su, and R. Zhang, Nucl. Phys. **B993**, 116282 (2023).
[19] J. Hua, M.-H. Chu, P. Sun, W. Wang, J. Xu, Y.-B. Yang, J.-H. Zhang, and Q.-A. Zhang (Lattice Parton Collaboration), Phys. Rev. Lett. **127**, 062002 (2021).
[20] J. Hua *et al.* (Lattice Parton Collaboration), Phys. Rev. Lett. **129**, 132001 (2022).
[21] E. Baker, D. Bollweg, P. Boyle, I. Cloët, X. Gao, S. Mukherjee, P. Petreczky, R. Zhang, and Y. Zhao, J. High Energy Phys. 07 (2024) 211.
[22] I. Cloet, X. Gao, S. Mukherjee, S. Syritsyn, N. Karthik, P. Petreczky, R. Zhang, and Y. Zhao, Phys. Rev. D **110**, 114502 (2024).
[23] V. L. Chernyak and A. R. Zhitnitsky, Nucl. Phys. **B201**, 492 (1982); **B214**, 547(E) (1983).
[24] J. Gronberg *et al.* (CLEO Collaboration), Phys. Rev. D **57**, 33 (1998).
[25] B. Aubert *et al.* (*BABAR* Collaboration), Phys. Rev. D **80**, 052002 (2009).
[26] S. Uehara *et al.* (Belle Collaboration), Phys. Rev. D **86**, 092007 (2012).
[27] L. Chang, I. C. Cloet, J. J. Cobos-Martinez, C. D. Roberts, S. M. Schmidt, and P. C. Tandy, Phys. Rev. Lett. **110**, 132001 (2013).
[28] Z.-F. Cui, M. Ding, F. Gao, K. Raya, D. Binosi, L. Chang, C. D. Roberts, J. Rodríguez-Quintero, and S. M. Schmidt, Eur. Phys. J. C **80**, 1064 (2020).
[29] C. D. Roberts, D. G. Richards, T. Horn, and L. Chang, Prog. Part. Nucl. Phys. **120**, 103883 (2021).
[30] V. L. Chernyak, A. A. Ogloblin, and I. R. Zhitnitsky, Yad. Fiz. **48**, 1410 (1988).
[31] G. S. Bali *et al.*, J. High Energy Phys. 02 (2016) 070.
[32] G. S. Bali *et al.* (RQCD Collaboration), Eur. Phys. J. A **55**, 116 (2019).
[33] X. Ji, Phys. Rev. Lett. **110**, 262002 (2013).
[34] X. Ji, Sci. China Phys. Mech. Astron. **57**, 1407 (2014).
[35] K. Orginos, A. Radyushkin, J. Karpie, and S. Zafeiropoulos, Phys. Rev. D **96**, 094503 (2017).
[36] A. V. Radyushkin, Phys. Rev. D **96**, 034025 (2017).
[37] Y.-Q. Ma and J.-W. Qiu, Phys. Rev. D **98**, 074021 (2018).
[38] X. Xiong, X. Ji, J.-H. Zhang, and Y. Zhao, Phys. Rev. D **90**, 014051 (2014).
[39] C. Alexandrou, K. Cichy, M. Constantinou, K. Hadjiyiannakou, K. Jansen, F. Steffens, and C. Wiese, Proc. Sci. LATTICE2016 (**2016**) 151 [arXiv:1612.08728].
[40] J.-W. Chen, T. Ishikawa, L. Jin, H.-W. Lin, J.-H. Zhang, and Y. Zhao (LP3 Collaboration), Chin. Phys. C **43**, 103101 (2019).
[41] J.-H. Zhang, L. Jin, H.-W. Lin, A. Schäfer, P. Sun, Y.-B. Yang, R. Zhang, Y. Zhao, and J.-W. Chen (LP3 Collaboration), Nucl. Phys. **B939**, 429 (2019).
[42] J. Xu, Q.-A. Zhang, and S. Zhao, Phys. Rev. D **97**, 114026 (2018).
[43] Y.-S. Liu, J.-W. Chen, L. Jin, R. Li, H.-W. Lin, Y.-B. Yang, J.-H. Zhang, and Y. Zhao, arXiv:1810.05043.
[44] W. Wang, Y.-M. Wang, J. Xu, and S. Zhao, Phys. Rev. D **102**, 011502(R) (2020).
[45] R. Zhang, Z. Fan, R. Li, H.-W. Lin, and B. Yoon, Phys. Rev. D **101**, 034516 (2020).
[46] L.-B. Chen, W. Wang, and R. Zhu, Phys. Rev. Lett. **126**, 072002 (2021).
[47] X. Ji, Y. Liu, A. Schäfer, W. Wang, Y.-B. Yang, J.-H. Zhang, and Y. Zhao, Nucl. Phys. **B964**, 115311 (2021).
[48] X. Ji, Y.-S. Liu, Y. Liu, J.-H. Zhang, and Y. Zhao, Rev. Mod. Phys. **93**, 035005 (2021).
[49] Q.-A. Zhang *et al.* (Lattice Parton Collaboration), Phys. Rev. Lett. **125**, 192001 (2020).
[50] H.-W. Lin, Phys. Rev. Lett. **127**, 182001 (2021).
[51] S. Bhattacharya, K. Cichy, M. Constantinou, A. Metz, A. Scapellato, and F. Steffens, Phys. Rev. D **104**, 114510 (2021).
[52] X. Gao, K. Lee, S. Mukherjee, C. Shugert, and Y. Zhao, Phys. Rev. D **103**, 094504 (2021).
[53] Y.-K. Huo *et al.* (Lattice Parton (LPC) Collaboration), Nucl. Phys. **B969**, 115443 (2021).
[54] Y. Li *et al.*, Phys. Rev. Lett. **128**, 062002 (2022).
[55] Z.-F. Deng, W. Wang, and J. Zeng, J. High Energy Phys. 09 (2022) 046.

[56] X. Gao, A. D. Hanlon, N. Karthik, S. Mukherjee, P. Petreczky, P. Scior, S. Shi, S. Syritsyn, Y. Zhao, and K. Zhou, Phys. Rev. D **106**, 114510 (2022).

[57] X. Gao, A. D. Hanlon, J. Holligan, N. Karthik, S. Mukherjee, P. Petreczky, S. Syritsyn, and Y. Zhao, Phys. Rev. D **107**, 074509 (2023).

[58] F. Yao *et al.* (Lattice Parton Collaboration), Phys. Rev. Lett. **131**, 261901 (2023).

[59] J.-C. He, M.-H. Chu, J. Hua, X. Ji, A. Schäfer, Y. Su, W. Wang, Y.-B. Yang, J.-H. Zhang, and Q.-A. Zhang (Lattice Parton Collaboration (LPC)), Phys. Rev. D **109**, 114513 (2024).

[60] M.-H. Chu *et al.* (Lattice Parton (LPC) Collaboration), Phys. Rev. D **106**, 034509 (2022).

[61] K. Zhang, X. Ji, Y.-B. Yang, F. Yao, and J.-H. Zhang (Lattice Parton (LPC) Collaboration), Phys. Rev. Lett. **129**, 082002 (2022).

[62] R. Zhu, Y. Ji, J.-H. Zhang, and S. Zhao, J. High Energy Phys. 02 (2023) 114.

[63] Z.-F. Deng, C. Han, W. Wang, J. Zeng, and J.-L. Zhang, J. High Energy Phys. 07 (2023) 191.

[64] X. Ji, Y. Liu, and Y. Su, J. High Energy Phys. 08 (2023) 037.

[65] M.-H. Chu *et al.* (Lattice Parton Collaboration), Phys. Rev. D **109**, L091503 (2024).

[66] Y. Zhao, Phys. Rev. Lett. **133**, 241904 (2024).

[67] Y. Liu and Y. Su, J. High Energy Phys. 02 (2024) 204.

[68] A. Avkhadiev, P. E. Shanahan, M. L. Wagman, and Y. Zhao, Phys. Rev. Lett. **132**, 231901 (2024).

[69] W. Good, K. Hasan, and H.-W. Lin, J. Phys. G **52**, 035105 (2025).

[70] C. Han, W. Wang, J.-L. Zhang, and J.-H. Zhang, Phys. Rev. D **110**, 094038 (2024).

[71] X.-Y. Han, J. Hua, X. Ji, C.-D. Lü, W. Wang, J. Xu, Q.-A. Zhang, and S. Zhao, Phys. Rev. D **111**, L111503 (2025).

[72] J. Holligan and H.-W. Lin, J. Phys. G **51**, 065101 (2024).

[73] J. Holligan and H.-W. Lin, Phys. Lett. B **854**, 138731 (2024).

[74] X. Ji, Y. Liu, Y. Su, and R. Zhang, J. High Energy Phys. 03 (2025) 045.

[75] W. Wang, J. Xu, Q.-A. Zhang, and S. Zhao, arXiv:2411.07101.

[76] X.-Y. Han *et al.* (Lattice Parton Collaboration), Phys. Rev. D **111**, 034503 (2025).

[77] K. Zhang, Y.-K. Huo, X. Ji, A. Schaefer, C.-J. Shi, P. Sun, W. Wang, Y.-B. Yang, and J.-H. Zhang (Lattice Parton Collaboration), Phys. Rev. D **110**, 074505 (2024).

[78] D. Bollweg, X. Gao, J. He, S. Mukherjee, and Y. Zhao, Phys. Rev. D **112**, 034501 (2025).

[79] W. Wang, J. Xu, Q.-A. Zhang, and S. Zhao, Phys. Rev. D **112**, 054044 (2025).

[80] Y. Ji, F. Yao, and J.-H. Zhang, arXiv:2504.09367.

[81] J.-W. Chen *et al.*, arXiv:2505.14619.

[82] A. V. Radyushkin, Phys. Lett. B **781**, 433 (2018).

[83] J.-H. Zhang, J.-W. Chen, and C. Monahan, Phys. Rev. D **97**, 074508 (2018).

[84] J. Karpie, K. Orginos, and S. Zafeiropoulos, J. High Energy Phys. 11 (2018) 178.

[85] B. Joó, J. Karpie, K. Orginos, A. Radyushkin, D. Richards, and S. Zafeiropoulos, J. High Energy Phys. 12 (2019) 081.

[86] B. Joó, J. Karpie, K. Orginos, A. V. Radyushkin, D. G. Richards, R. S. Sufian, and S. Zafeiropoulos, Phys. Rev. D **100**, 114512 (2019).

[87] C. Egerer *et al.* (HadStruc Collaboration), Phys. Rev. D **105**, 034507 (2022).

[88] M. Bhat, W. Chomicki, K. Cichy, M. Constantinou, J. R. Green, and A. Scapellato, Phys. Rev. D **106**, 054504 (2022).

[89] D. Kovner, J. Karpie, K. Orginos, A. Radyushkin, and S. Zafeiropoulos (HadStruc Collaboration), Proc. Sci. LATTICE2023 (**2024**) 300 [arXiv:2401.06858].

[90] S. Bhattacharya, K. Cichy, M. Constantinou, A. Metz, N. Nurminen, and F. Steffens, Phys. Rev. D **110**, 054502 (2024).

[91] H. Dutrieux, R. G. Edwards, C. Egerer, J. Karpie, C. Monahan, K. Orginos, A. Radyushkin, D. Richards, E. Romero, and S. Zafeiropoulos (HadStruc Collaboration), J. High Energy Phys. 08 (2024) 162.

[92] A. NieMiera, W. Good, and H.-W. Lin, Phys. Rev. D **112**, 074504 (2025).

[93] G. S. Bali *et al.*, Eur. Phys. J. C **78**, 217 (2018).

[94] R. S. Sufian, J. Karpie, C. Egerer, K. Orginos, J.-W. Qiu, and D. G. Richards, Phys. Rev. D **99**, 074507 (2019).

[95] G. S. Bali, V. M. Braun, B. Gläßle, M. Göckeler, M. Gruber, F. Hutzler, P. Korcyl, A. Schäfer, P. Wein, and J.-H. Zhang, Phys. Rev. D **98**, 094507 (2018).

[96] R. S. Sufian, C. Egerer, J. Karpie, R. G. Edwards, B. Joó, Y.-Q. Ma, K. Orginos, J.-W. Qiu, and D. G. Richards, Phys. Rev. D **102**, 054508 (2020).

[97] C. Zimmermann and A. Schäfer, Phys. Rev. D **110**, 074503 (2024).

[98] M.-H. Chu *et al.* (Lattice Parton Collaboration), Phys. Rev. D **111**, 034510 (2025).

[99] V. M. Braun, S. E. Derkachov, G. P. Korchemsky, and A. N. Manashov, Nucl. Phys. **B553**, 355 (1999).

[100] C. Han, W. Wang, J. Zeng, and J.-L. Zhang, J. High Energy Phys. 07 (2024) 019.

[101] X. Gao, A. D. Hanlon, S. Mukherjee, P. Petreczky, P. Scior, S. Syritsyn, and Y. Zhao, Phys. Rev. Lett. **128**, 142003 (2022).

[102] C.-Y. Chou and J.-W. Chen, Phys. Rev. D **106**, 014507 (2022).

[103] J. Hua, M.-H. Chu, P. Sun, W. Wang, J. Xu, Y.-B. Yang, J.-H. Zhang, and Q.-A. Zhang (Lattice Parton (LPC) Collaboration), Proc. Sci. LATTICE2021 (**2022**) 322.

[104] Y. Su, J. Holligan, X. Ji, F. Yao, J.-H. Zhang, and R. Zhang, Nucl. Phys. **B991**, 116201 (2023).

[105] X. Ji, Research **8**, 0695 (2025).

[106] X. Gao, A. D. Hanlon, S. Mukherjee, P. Petreczky, P. Scior, S. Syritsyn, and Y. Zhao, Proc. Sci., LATTICE2022 (**2023**) 104.

[107] F. Yao, Y. Ji, and J.-H. Zhang, J. High Energy Phys. 11 (2023) 021.

[108] R. Zhang, Lattice quantum chromodynamics (QCD) calculations of parton physics with leading power accuracy in large momentum expansion, Ph.D. thesis, Maryland University, College Park, 2023.

[109] R. Zhang, J. Holligan, X. Ji, and Y. Su, Phys. Lett. B **844**, 138081 (2023).

[110] X. Gao, W.-Y. Liu, and Y. Zhao, Phys. Rev. D **109**, 094506 (2024).
[111] C. Chen, Y. Geng, L. Liu, P. Sun, Y.-B. Yang, F. Yao, J.-H. Zhang, and K. Zhang (CLQCD, Lattice Parton Collaboration), Phys. Rev. D **111**, 074506 (2025).
[112] J. Holligan, H.-W. Lin, R. Zhang, and Y. Zhao, J. High Energy Phys. 07 (2025) 241.
[113] W. Good, F. Yao, and H.-W. Lin, Phys. Lett. B **872**, 140067 (2026).
[114] C. Han, Y. Su, W. Wang, and J.-L. Zhang, J. High Energy Phys. 12 (2023) 044.
[115] C. Han and J. Zhang, Phys. Rev. D **109**, 014034 (2024).
[116] J.-W. Chen, X. Ji, and J.-H. Zhang, Nucl. Phys. **B915**, 1 (2017).
[117] X. Ji, J.-H. Zhang, and Y. Zhao, Phys. Rev. Lett. **120**, 112001 (2018).
[118] T. Ishikawa, Y.-Q. Ma, J.-W. Qiu, and S. Yoshida, Phys. Rev. D **96**, 094019 (2017).
[119] J. Green, K. Jansen, and F. Steffens, Phys. Rev. Lett. **121**, 022004 (2018).
[120] X.-D. Ji, arXiv:hep-ph/9507322.
[121] M. Beneke, Phys. Rep. **317**, 1 (1999).
[122] C. Bauer, G. S. Bali, and A. Pineda, Phys. Rev. Lett. **108**, 242002 (2012).
[123] G. S. Bali, C. Bauer, A. Pineda, and C. Torrero, Phys. Rev. D **87**, 094517 (2013).
[124] Z.-C. Hu *et al.* (CLQCD Collaboration), Phys. Rev. D **109**, 054507 (2024).
[125] Y. Aoki *et al.* (Flavour Lattice Averaging Group (FLAG) Collaboration), arXiv:2411.04268.
[126] Y.-K. Huo *et al.* (Lattice Parton (LPC) Collaboration), Nucl. Phys. **B969**, 115443 (2021).
[127] H. Liu, J. He, L. Liu, P. Sun, W. Wang, Y.-B. Yang, and Q.-A. Zhang, Sci. China Phys. Mech. Astron. **67**, 211011 (2024).
[128] H. Xing, J. Liang, L. Liu, P. Sun, and Y.-B. Yang, arXiv:2210.08555.
[129] H. Yan, C. Liu, L. Liu, Y. Meng, and H. Xing, Phys. Rev. D **111**, 014503 (2025).
[130] Q.-A. Zhang, J. Hua, Fei Huang, R. Li, Y. Li, C. Lü, P. Sun, W. Sun, W. Wang, and Y. Yang, Chin. Phys. C **46**, 011002 (2022).
[131] H. Liu, W. Wang, and Q.-A. Zhang, Phys. Rev. D **109**, 036037 (2024).
[132] G. S. Bali, B. Lang, B. U. Musch, and A. Schäfer, Phys. Rev. D **93**, 094515 (2016).
[133] A. Hasenfratz and F. Knechtli, Phys. Rev. D **64**, 034504 (2001).
[134] T. A. DeGrand, A. Hasenfratz, and T. G. Kovacs, Phys. Rev. D **67**, 054501 (2003).
[135] R. Zhang, A. V. Grebe, D. C. Hackett, M. L. Wagman, and Y. Zhao, Phys. Rev. D **112**, L051502 (2025).
[136] W. I. Jay and E. T. Neil, Phys. Rev. D **103**, 114502 (2021).
[137] A.-S. Xiong, J. Hua, T. Wei, F.-S. Yu, Q.-A. Zhang, and Y. Zheng, arXiv:2506.16689.
[138] X. Jiang, C. Shi, Y. Chen, M. Gong, and Y.-B. Yang, arXiv:2411.08461.
[139] M. A. Clark, R. Babich, K. Barros, R. C. Brower, and C. Rebbi (QUDA Collaboration), Comput. Phys. Commun. **181**, 1517 (2010).
[140] R. Babich, M. A. Clark, B. Joo, G. Shi, R. C. Brower, and S. Gottlieb (QUDA Collaboration), in *International Conference for High Performance Computing, Networking, Storage and Analysis* (2011), 10.1145/2063384.2063478.
[141] M. A. Clark, B. Joó, A. Strelchenko, M. Cheng, A. Gambhir, and R. C. Brower (QUDA Collaboration), in *International Conference for High Performance Computing, Networking, Storage and Analysis* (2016), 10.5555/3014904.3014995.
[142] Y.-J. Bi, Y. Xiao, W.-Y. Guo, M. Gong, P. Sun, S. Xu, and Y.-B. Yang, Proc. Sci., LATTICE2019 (**2020**) 286 [arXiv:2001.05706].
[143] V. Braun, R. J. Fries, N. Mahnke, and E. Stein, Nucl. Phys. **B589**, 381 (2000); **B607**, 433(E) (2001).